

Towards quantitative super-resolution microscopy: Molecular maps with statistical guarantees

KATHARINA PROKSCH¹

`k.proksch@utwente.nl`

Faculty of Electrical Engineering, Mathematics and Computer Science,
Universiteit Twente, Enschede, The Netherlands

FRANK WERNER¹

`frank.werner@mathematik.uni-wuerzburg.de`

Institute of Mathematics, University of Würzburg, Germany

JAN KELLER-FINDEISEN¹

`jan.keller@mpinat.mpg.de`

Max-Planck-Institut für multidisziplinäre Naturwissenschaften, Göttingen,
Germany

HAISEN TA

`hta@pysnet.uni-hamburg.de`

Center for Hybrid Nanostructures, Universität Hamburg, Germany

AXEL MUNK

`munk@math.uni-goettingen.de`

Institute for Mathematical Stochastics, University of Göttingen
and

Felix Bernstein Institute for Mathematical Statistics in the Bioscience,
University of Göttingen

and

Max-Planck-Institut für multidisziplinäre Naturwissenschaften, Göttingen,
Germany

Quantifying the number of molecules from fluorescence microscopy measurements is an important topic in cell biology and medical research. In this work, we present a consecutive algorithm for super-resolution (STED) scanning microscopy that provides molecule counts in automatically generated image segments and offers statistical guarantees in form of asymptotic confidence intervals. To this end, we first apply a multiscale scanning procedure on STED microscopy measurements of the sample to obtain a system of significant regions, each of which contains at least one molecule with prescribed uniform probability. This system of regions will typically be highly redundant and consists of rectangular building blocks. To choose an informative but non-redundant subset of more naturally shaped regions, we hybridize our system with the result of a generic segmentation algorithm. The diameter of the segments can be of the order of the resolution of the microscope. Using multiple photon coincidence measurements of the same sample in confocal mode, we are then able to estimate the brightness and number of the molecules and give uniform confidence intervals on the molecule counts for each previously constructed segment. In other words, we establish a so-called *molecular map* with uniform error control. The performance of the algorithm is investigated on simulated and real data.

¹These authors contributed equally

Keywords: asymptotic normality, counting, family-wise error rate, molecular map, multiplicity adjustment, super-resolution microscopy.

AMS classification numbers: 60K35.

1. Introduction

1.1. Super-resolution microscopy

In fluorescence microscopy, structures of interest inside a specimen are labeled with fluorescent markers and then imaged using visible light illumination. Only the fluorescence itself and thus the labeled structures are detected, making it possible, for example, to investigate details inside living cells with unrivaled contrast. The tremendous development of super-resolution fluorescence microscopy in recent decades has extended spatial resolution beyond the diffraction limit of conventional microscopy to the nanometer scale. Nowadays, even temporal dynamics in living cells can be observed in 3D with high spatial resolution.

All super-resolution light microscopy concepts rely on distinguishing fluorophores locally by consecutively transferring them between a dark (non-fluorescent) and a bright (fluorescent) state using light to induce these transitions (Hell, 2007; Sahl et al., 2017). The transitions between these states can be performed either in a spatially controlled or in a stochastic manner, with the latter denoted here as single-molecule switching (SMS) microscopy (Betzig et al., 2006). In both approaches only a small subset of molecules is left in the bright state at each measurement step and the final image is assembled by repeating the experiment many times. A well established spatially controlled method uses stimulated emission depletion (STED) (Hell and Wichmann, 1994; Klar et al., 2000). Thereby a red-shifted light spot featuring a central intensity minimum is co-aligned with the excitation light spot. It induces strongly saturated stimulated emission, effectively inhibiting the fluorophores from emitting fluorescence in the periphery of a focused excitation light spot. The very small spot of effectively allowed fluorescence emission can be scanned over the sample to deliver a final image. For example, the STED principle has been used in the past to reveal the distribution of synaptic proteins in living mice (Masch et al., 2018) or the dynamics of membrane lipids in living cells (Eggeling et al., 2009). Recently, a combination of stochastic switching and excitation light patterns with at least one isolated intensity zero, called MINFLUX, was used to achieve isotropic resolution on the order of a few nanometers (Balzarotti et al., 2016).

From a statistical perspective, the recovery of spatial intensity and specimen distribution from super-resolution fluorescence microscopy images leads to sophisticated convolution models with Poisson or Binomial data distributions, which in themselves present a number of challenges (see, e.g., Aspelmeier et al. (2015); Hohage and Werner (2016); Munk et al. (2020b); Kulaitis et al. (2021) and references therein).

In many biological contexts, however, it is not only the precise localization of structures that is of interest, but also the determination of the exact number of fluorescent markers at a given location, especially if this number can be related to the local number of proteins or other biological targets of interest. Such quantitative knowledge of target structures at the nanoscale has the potential to greatly improve the understanding of many biological processes. Knowledge of the absolute number of molecules can provide the basis for structural models of protein complexes or determine thresholds for the number of molecules required to produce a particular effect. For example, estimating the number of constituent proteins in kinetochores reported unexpectedly high numbers of proteins present (Coffman et al., 2011), whereas quantifying the number of proteins used for flagellar regeneration helped refine models for flagellar assembly (Engel et al., 2009).

1.2. Towards molecule counting

In general, the mean recorded fluorescence signal in a microscope is proportional to the number of active fluorescent markers. If we denote by f_N a spatial function assigning each location (or pixel) the corresponding number of markers, and by f_p their corresponding brightness (i.e., probability to emit a photon after an excitation pulse was applied), then the observed quantity is mathematically given by a spatial convolution of the product $f_N \cdot f_p$ with the so-called point spread function (PSF) h , which is determined by the microscope (see Section 2 below for details). This already shows that the measurements cannot be readily used to infer the absolute number of markers, since each fluorophore has its own (unknown) brightness and thus f_p is unknown. If the microscope could guarantee that each fluorophore was perfectly separated, counting fluorophores would be a trivial task, but in almost all current applications this is not the case. Robust statistical modeling of the contributions of the fluorophores to the acquired image data, and, in particular, a method for calibrating the brightness of a single molecule, are therefore required. This calibration is ideally performed during the measurement itself, since the molecular brightness can change depending on the microscope configuration used and the sample conditions.

In the super-resolution techniques that leave only isolated markers in the bright state (as it is e.g. the case in SMS microscopy), counting can be performed by a careful analysis of the localization events (see e.g. Lee et al., 2012; Rollins et al., 2015; Hummer et al., 2016; Staudt et al., 2020). From a statistical perspective this is mainly based on the *temporal* Markovian dynamics of the transition between bright and dark states of the fluorophores (Patel et al., 2019; Gabitto et al., 2021).

In case of *spatially* separating super-resolution microscopy, e.g. for STED as considered in this work, a similar approach is not possible. Instead, the single molecule brightness has traditionally been estimated by observing single photo bleaching steps, which is challenging in dense samples. For the case of repeatedly activatable markers one can also determine an excess variance, which was used to determine the molecule brightness (Park et al., 2005; Frahm et al., 2019). Despite its practical relevance, stochastically sound methods for counting molecules from scanning microscopy images remain elusive until nowadays.

1.3. Our approach

In this work, we will address this issue by means of a different path. To this end, we will perform counting based on the photon emission statistics, specifically the number of photons that are emitted simultaneously. This has recently emerged as a tool for intrinsically calibrating the molecular brightness and to infer on the number of molecules present. The physical effect that affects the photon emission statistics is photon antibunching, i.e., an excited fluorophore cannot emit more than one photon during the lifetime of the excited state. First measurements showed that the number of markers can be inferred from the photon emission statistics (Ta et al., 2010). Termed antibunching microscopy, it has been implemented later in STED mode and could for example count the number of internalized receptors within small vesicles in HEK293 cells (Ta et al., 2015). This technique is able to account for locally varying molecular brightness. Mathematically, this leads to observations proportional to $f_N \cdot f_p$, $f_N \cdot f_p^2$, ..., which in principle allows decoupling the (local) number of markers f_N from their brightness f_p . A scheme of an antibunching STED microscope is shown in Figure 1. It provides simultaneous detections of multiple photons, i.e., the measurement of photon coincidences. State of the art single photon detectors (avalanche photo diodes) still feature considerable times where they are insensitive after each photon detection (on the order of 50 nanoseconds), rendering them incapable of detecting photon coincidences. This limitation is effectively overcome by parallel detection, i.e., by splitting the emitted light equally among multiple detectors.

At each scan position (the scan covers the whole sample equally) a fixed number t of excitation light pulses are applied and the statistics of detected number of photons is recorded. This can be seen as repetitions of a multinomial experiment with an additional twist that photons arriving at the same detector are only registered as a single detection event. The accessible observable is

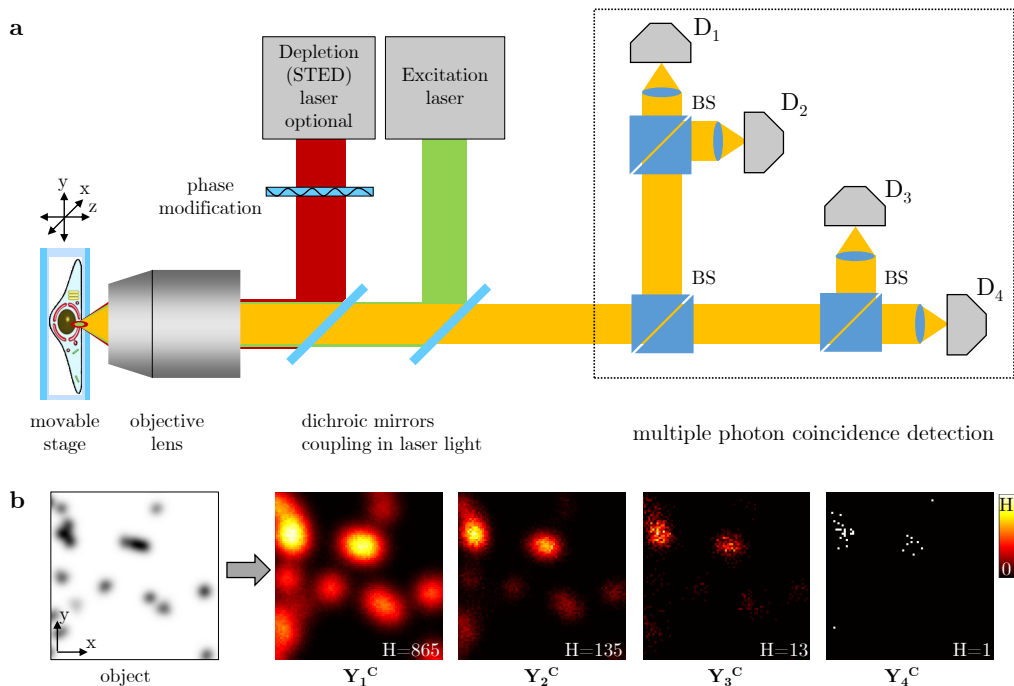


Figure 1: **Microscope scheme and example images for detecting multiple photon coincidences.** **a** Schematic of a confocal/STED fluorescence light microscope capable of detecting multiple photon coincidences. Excitation, depletion and fluorescence light are combined with dichroic mirrors. A specific phase distribution is imprinted on the depletion beam in order to create a doughnut shaped intensity distribution of depletion light at the focal point. Effectively, the spot in the sample that is allowed to fluoresce is reduced to a sub-diffraction extent. In the detection unit, the fluorescence light is split by three beam splitters (BS) in four equal intensity paths and directed on four identical detectors ($D_i, i = 1, \dots, 4$). Such a microscope has been built and used for antibunching microscopy in (Ta et al., 2015). **b** Example object (molecule density) and corresponding simulated photon coincidence measurement images $Y_i^C, i = 1, \dots, 4$ in confocal mode (excitation pulses per pixel $t = 3000$), see Section 2 for details on model and data. The scaling of the colorbar is indicated by the value H in each image.

indeed only the number of active detectors for each excitation light pulse, which depends on the number of emitted photons and the number of the available detectors. In Section 2, we develop an explicit multinomial model that encodes the photon emission and detection probabilities and is given by convolutions and products of the local brightness, the local number of markers, and the effective point spread function of the microscope itself. The accuracy of the estimation of the multinomial probabilities of our model increases with increasing number t of excitation light pulses. Therefore, our theoretical considerations assume an asymptotic viewpoint as this number tends to infinity. Utilizing this model, measuring multiple photon coincidences allows for inference on the (local) number of markers, as the simultaneous arrival of two photons at a certain scan position implies that the two photons must originate from at least two different fluorophores. We will show later on, that the empirical distribution of the number of active detectors depends uniquely on the number and location of molecules present. An estimation of the local molecular number and brightness by a penalized maximum likelihood based reconstruction algorithm (without statistical guarantees) was implemented in Ta et al. (2015). Besides lack of statistical guarantees for the local molecular numbers, the statistical model therein is limited to two simultaneously arriving photons at most.

1.4. Our contribution

As the goal of counting the number of fluorescent markers in a sample would greatly benefit from both being able to calculate error bounds on the numbers and considering higher order photon coincidences, in this work, we will extend the existing approach in these directions. First of all, we derive a detailed and sound statistical model for the observations obtained from the antibunching microscope including contributions of arbitrarily high photon coincidences. One major contribution is that instead of globally estimating the number of markers inside the specimen, we construct a so-called *molecular map* with uniform error control. This is a collection of family-wise error rate (FWER) controlled, distinct segments in the specimen together with uniform confidence intervals for the number of markers contained in each segment. The diameter of these segments can be of the order of the resolution of the microscope. To derive this molecular map with a given total error level $\alpha \in (0, 1)$, the method performs three steps:

- S1: Segmentation.** We first construct a segmentation of the image space such that each segment contains at least one molecule with uniform probability at least $1 - \alpha/2$ and, at the same time, has a suitable shape. All image pixels that are not contained in any of the segments are no longer considered in steps S2 and S3.
- S2: Estimation.** Given M (say) segments from S1, we estimate (locally) the number of molecules, i.e. segment by segment.
- S3: Confidence.** Based on a central limit theorem, we construct $1 - \alpha/(2M)$ confidence intervals for each of the M local (segment-wise) numbers of molecules.

The outcome of this procedure is a collection of distinct segments, estimated marker counts in these segments and confidence intervals (CIs) such that asymptotically (as the number t of excitation light pulses tends to infinity) the following statement is true (see Theorem 4.2):

$$\mathbb{P}[\text{Each CI contains the correct number of markers in its segment}] \geq 1 - \alpha. \quad (1.1)$$

We provide MATLAB[®] code for the approach described above under

https://github.com/jkfindeisen/antibunching_microscopy_analysis_2022

and investigate its performance in numerical simulations as well as real data examples in Sections 5 and 6.

Let us discuss some immediate issues and the rationale behind this three step approach. In principle, the measured photon coincidences do allow for a pixel-wise estimation of the number of markers, and hence also for pixel-wise confidence statements. This is also possible with the above three step approach by considering each pixel as a separate segment. However, to obtain a uniform coverage as in (1.1), the corresponding confidence intervals (e.g. as constructed in step S3) will then be unfavorably large due to the large number of pixels (in practical applications of the order $10^5 - 10^6$) and its corresponding multiplicity correction. To overcome this burden, we exploit the fact that in many samples the molecules are concentrated on parts of the measurement volume and our algorithm estimates on relevant regions only. Consequently, it neglects a substantial fraction of all pixels before performing the estimation. If the segments are still chosen reasonably small (e.g. in the order of the microscope resolution rather than single pixels), local information is maintained while at the same time the number of confidence statements to be made is reduced significantly. Therefore, a reasonable segmentation in step S1 will strongly ease the estimation and confidence procedure afterwards. Such a segmentation will be achieved by a hybridization of an established segmentation approach from image processing such as, e.g., the watershed segmentation, with the **M**ultiscale **I**nverse **S**Canning **T**est (MISCAT) procedure introduced in Proksch et al. (2018), which is a method based on multiple statistical hypothesis testing. Note, that even though the number M of segments in step S2 is random, this does not cause problems in step S3, as it can be considered deterministic conditional on the data used for step S1. Moreover, in our asymptotic considerations, the number of pixels, which is an upper bound for M , is fixed.

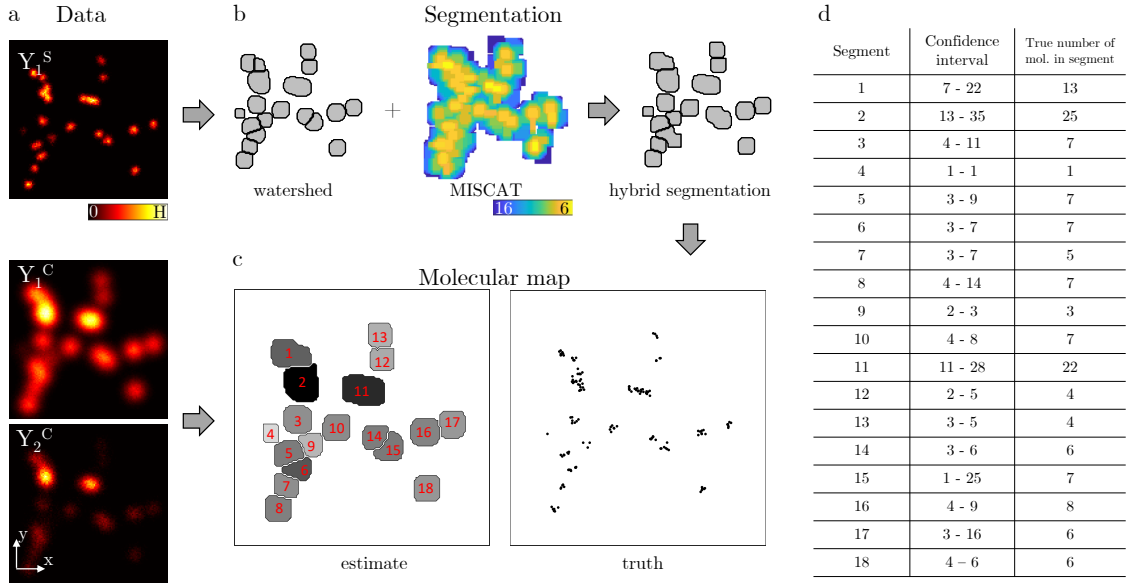


Figure 2: **Three step analysis workflow.** **a** Simulated one photon STED image with high spatial resolution (top left) and one and two photon detection images in confocal mode (center left and bottom left) for the example object depicted in Fig. 1b. **b** The STED image Y_1^S is used for a combined watershed and MISCAT segmentation that results in an effective hybrid segmentation, where each segment contains at least one molecule with uniform probability. Color-scale for MISCAT is inverse to box area and smaller boxes are drawn on top of larger boxes. **c** Using the one and two photon statistics obtained in confocal mode $Y_{1,2}^C$ and the hybrid segmentation in b, the number of molecules and confidence bounds can be obtained for each segment. The segments are enumerated (red) and the fill color (on a gray scale) indicates the estimated local molecule density within a segment. The true location of markers is shown on the right. **d** Segment number, confidence bounds ($\alpha = 0.1$) and true number of molecules for each of the 18 obtained segments.

The three step approach is visualized in Figure 2. In the example shown there, the images have $512 \times 512 = 262,144$ pixels, but M , the number of identified segments containing markers, is only 18.

We investigate the introduced methodology both in simulations and on experimental data. The former gives a precise description of the abilities and limitations, and the latter shows the high practical value of our approach.

The remainder of the paper is organized as follows: In Section 2 we state the statistical model for raw photon counts in antibunching microscopy and their relation to the local number of markers inside the sample. The technical derivation of this model is put to an appendix. Sections 3, 4 and 5 are devoted to the three steps of our inference algorithm. In Section 6 we illustrate the performance in numerical simulations, and in Section 7 we discuss the applicability on real world data. We end with a short conclusion in Section 7.

2. Modelling, notation and prerequisites

Throughout this work, we denote by $[n]$ the set $\{1, \dots, n\}$. Vectors and multi-indices will be written in bold face, where, with a slight abuse of notation, we denote the vector of component-wise ratios i_k/n_k by \mathbf{i}/\mathbf{n} .

In the following, we denote by N the total (unknown) number of fluorescent markers in our

specimen of interest. W.l.o.g. we can assume that all markers are contained in the unit square $[0, 1]^2$, which is discretized by the grid

$$\mathbf{x}_{(i_1, i_2)} = \mathbf{x}_{\mathbf{i}} = \left(\frac{i_1}{n}, \frac{i_2}{n} \right), \quad \mathbf{i} \in [n] \times [n].$$

The j th marker has a position $\mathbf{x}_{\psi(j)}$ on this grid (where the true position is just assigned to the closest grid point), which is encoded in terms of the mapping $\psi : [N] \rightarrow [n] \times [n]$ that assigns to the j -th marker, $j \in [N]$, its position on the grid. Furthermore, the j -th marker has an individual brightness p_j . The individual brightness of a marker j is its probability to collect a photon after an excitation light pulse focused to $\mathbf{x}_{\psi(j)}$ was applied, see, e.g., [Aspelmeier et al. \(2015\)](#).

The antibunching microscope shown in [Figure 1](#) works as follows. The specimen is scanned spatially along the grid $\mathbf{x}_{\mathbf{i}}, \mathbf{i} \in [n] \times [n]$. For each grid point $\mathbf{x}_{\mathbf{i}}$, the following experiment is repeated a total number of t times: A short excitation pulse with a duration much shorter than the excited state's lifetime is applied to the sample (focused on the current grid point $\mathbf{x}_{\mathbf{i}}$), and afterwards the fluorescence is recorded at the detectors. Between two experiments, there is a certain waiting time, which takes into account the dead-time of the detectors after recording a photon (typically around 100 nanoseconds) and the typical fluorescence lifetime of the markers (typically ≤ 10 nanoseconds). In each experiment, the number of detected photons, k , is recorded.

It is important to note that a pulse centered at the point \mathbf{x} will also illuminate neighbouring grid points due to diffraction, however, with a lower intensity. This implies that the probability $\mathbf{p}_j(\mathbf{x})$ to detect an emission from the j -th marker in a single excitation pulse when scanning at position $\mathbf{x} \in [0, 1]^2$ is given by

$$\mathbf{p}_j(\mathbf{x}) = p_j \cdot h(\mathbf{x} - \mathbf{x}_{\psi(j)}). \quad (2.1)$$

Here, h is point spread function of the microscope, which reaches its maximal value at 0, and therefore a detection at the correct position is most likely. However, relation [\(2.1\)](#) shows that markers collectively contribute to the measured signal at a specific scanning position \mathbf{x} , even though they are located at different grid points. The shape of h depends on various experimental parameters in the microscope. As a rough guidance, h has a larger extent when using conventional (i.e. not super-resolved) microscopy (as more surrounding markers are also excited), and a smaller extend in case of STED measurements corresponding to a smaller or larger resolution. An often used measure describing the shape of h and also of the microscope's resolution is its full width at half maximum (FWHM), cf. [Kulaitis et al. \(2021\)](#) for an explanation in statistical terms. In case of a Gaussian peak PSF h with variance σ^2 , one has $\text{FWHM} = 2\sqrt{2 \log 2} \sigma$.

As a consequence of [\(2.1\)](#), we obtain by superposition a convolution model

$$g(\mathbf{x}) = \sum_{j=1}^N \mathbf{p}_j(\mathbf{x}) = \int_{[0,1]^2} f_N(\mathbf{y}) f_p(\mathbf{y}) h(\mathbf{x} - \mathbf{y}) \, d\mathbf{y}, \quad (2.2)$$

where $g(\mathbf{x})$ denotes the probability to detect at least one photon when scanning at $\mathbf{x} \in [0, 1]^2$, f_N denotes the spatial number of markers and f_p their brightness at $\mathbf{x} \in [0, 1]^2$.

The convolution model in [\(2.2\)](#) is most commonly used for standard fluorescence microscopes to recover the product $f_N \cdot f_p$, see e.g. [Aspelmeier et al. \(2015\)](#). However, our modified microscope sketched in [Figure 1](#) does not only measure the total number of photons when scanning at $\mathbf{x}_{\mathbf{i}}, \mathbf{i} \in [n] \times [n]$, but furthermore measures the number of coincidences, i.e., k detected photons at the same time for $0 \leq k \leq m_d$, where m_d denotes the number of parallel detector units present in the microscope (see [Figure 1](#)). This allows to finally decouple f_N and f_p . The data for the current grid point $\mathbf{x}_{\mathbf{i}}$ consequently consists of integers $Y_{\mathbf{i}}^k$ being the number of k -photon events at $\mathbf{x}_{\mathbf{i}}$, $0 \leq k \leq m_d$. This immediately implies that our (ideal) data will consist of (pixel-wise) multinomial observations, i.e.

$$\mathbf{Y}_{\mathbf{i}} = (Y_{\mathbf{i}}^0, \dots, Y_{\mathbf{i}}^{m_d}) \sim \mathcal{M}(t, D_0(\mathbf{x}_{\mathbf{i}}), \dots, D_{m_d}(\mathbf{x}_{\mathbf{i}})), \quad \mathbf{i} \in [n] \times [n], \quad (2.3)$$

where \mathcal{M} denotes the multinomial distribution with a total number of t experiments per image pixel, and the numbers $D_k(\mathbf{x}_i)$ denote the probabilities to observe k photons at position \mathbf{i} . Note, that in the notation of (2.2), we have that

$$g(\mathbf{x}_i) = \sum_{k \geq 1} D_k(\mathbf{x}_i).$$

Throughout this work, we assume that the observations for different grid points \mathbf{x}_i are independent, which means that we assume that the observations $\mathbf{Y}_i, \mathbf{i} \in [n]^2$ are independent, multinomially distributed random variables. This is a reasonable assumption as long as markers come not so close to each other that they interact. Note that model (2.3) does not incorporate external noise sources such as detector read-out errors. However, such statistical thinning as it might be caused by loss of photons in the detectors can be included by re-defining the brightness p_j of the individual molecules, cf. Munk et al. (2020b). In conclusion, the model (2.3) can be considered as highly accurate if the number of repetitions per pixel, t , is of the order of several thousands, which corresponds to typical experimental conditions.

A detailed model for the probabilities $D_k, k = 0, \dots, m_d$, in dependence on the unknown quantities of interest such as the local number of markers f_N and their brightness f_p is developed in Appendix Proofs. To describe it briefly, let us introduce the function $\mathbf{s} : [0, 1]^2 \rightarrow \mathbb{R}^{m_d}$, defined by

$$\begin{aligned} \mathbf{s}(\mathbf{x}_i) &= \left(\sum_{j=1}^N (\mathbf{p}_j(\mathbf{x}_i))^k \right)_{k=1, \dots, m_d} \\ &= \left(\int_{[0,1]^2} f_N(\mathbf{x}) f_p(\mathbf{x})^k h(\mathbf{x} - \mathbf{x}_j)^k d\mathbf{x} \right)_{k=1, \dots, m_d}. \end{aligned} \quad (2.4)$$

Then, \mathbf{s} can be related to the probabilities \mathbf{D} – which can themselves be estimated from the available observations – as stated in the following theorem.

Theorem 2.1 (Statistical model for the antibunching microscope). *Let m_d denote the number of detectors, N the total number of fluorescent markers in the specimen and $\kappa = \kappa(\mathbf{x})$ the number of emitted photons in one excitation pulse at position \mathbf{x} . Assume that $N > m_d$. Let*

$$\mathbf{D}(\mathbf{x}_i) := (D_0(\mathbf{x}_i), \dots, D_{m_d}(\mathbf{x}_i))$$

denote the multinomial probabilities defined in model (2.3). Assume that, for any $\mathbf{x} \in [0, 1]^2$, there exists a $\gamma = \gamma(\mathbf{x}) \in (0, 1)$ such that for any $k > m_d$ it holds that

$$\mathbb{P}(\geq \kappa \text{ photons emitted at position } \mathbf{x} \text{ during one pulse}) \leq \gamma^\kappa. \quad (2.5)$$

Then there exists an explicitly known differentiable, invertible map $\mathbf{T} : [0, 1]^{m_d} \rightarrow \mathbb{R}^{m_d}$ such that

$$\mathbf{D}(\mathbf{x}_i) = \mathbf{T}(\mathbf{s}(\mathbf{x}_i)) + O(\gamma^{m_d+1}) \quad \text{as } \gamma \rightarrow 0. \quad (2.6)$$

For an explicit formula for \mathbf{T} , see the proof of Theorem 2.1.

Note that assumption (2.5) will be satisfied as soon as the local number of molecules around a position \mathbf{x} and / or their brightness is not too large compared to the number of detectors m_d . As a consequence, for sufficiently large m_d , we can neglect the remainder term in (2.6) and obtain (approximately) a non-linear forward model

$$(D_k)_{0 \leq k \leq m_d} = F(f_N, f_p), \quad (2.7)$$

with F given by the concatenation of \mathbf{T} and the mapping $(f_N, f_p) \mapsto \mathbf{s}$ (recall (2.4)), from which we aim to determine local information on the spatial number f_N (and the spatial brightness f_p) of molecules from empirical measurements \mathbf{Y} as in (2.3). This can be seen as a nonlinear inverse problem, which is also ill-posed due to the PSF h .

Note that the model (2.7) completely ignores background contributions, e.g. from out-of-focus planes. This is for simplicity mostly, as the following considerations can immediately be adjusted to a spatially varying background intensity λ , which, however, leads to even more technical results. In principle this would allow to determine not only f_N and f_p from the available data, but also λ . In practice, this corresponds to a highly underdetermined problem, which is why typically the background intensity is pre-estimated and then used to correct the data. To keep the theory concise, we have therefore decided to neglect all background contributions for the sake of simplicity here. A more refined model including the estimation of λ is presented in the implementation only (cf. Section 6).

In practice, we are able to obtain the measurements \mathbf{Y} in different imaging modes. As shown in Figure 1, the microscope has an additional STED laser, which can either be turned on or off, yielding different effective PSFs h . This allows us to image the specimen once via classical confocal microscopy (where the STED laser is turned off) and once via super-resolution STED microscopy. The properties, advantages and disadvantages of both imaging modes will be discussed in more detail later on. In total, this means that we collect and analyze both STED data $\mathbf{Y}_i^S = (Y_i^{S,0}, \dots, Y_i^{S,m_d})$ (consisting of the corresponding k -photon counts for $0 \leq k \leq m_d$) as well as confocal data $\mathbf{Y}_i^C = (Y_i^{C,0}, \dots, Y_i^{C,m_d})$.

3. Segmentation

If we tried to construct pixel-wise confidence intervals for the local number of molecules everywhere in the image (comparable to (1.1)), we would not obtain meaningful results due to the large number of pixels, as the necessary multiplicity adjustments would inflate the results. Therefore, it is important to first neglect uninteresting (e.g. empty) parts of the image, and to count not pixel-wise but in regions of interest (RoIs), which need to be determined based on the data as well. The proper selection of RoIs can be seen as a segmentation problem: The image has to be segmented into 'active' regions (i.e. containing molecules) and 'inactive' regions (i.e. containing no or only very few molecules), and afterwards estimation will be performed only in the 'active' regions. To make this useful, we aim to select a system of RoIs such that

- (R1) all interesting clusters of molecules are contained in one of the RoIs,
- (R2) with high probability each RoI contains at least one molecule,
- (R3) the RoIs do not intersect (i.e. form a segmentation),
- (R4) the RoIs are reasonably small and
- (R5) the RoIs have suitable shapes.

The above goals do not necessarily align in a certain sense. A usual approach would be to use a standard data-driven segmentation algorithm on the STED data $\mathbf{Y}^{S,1}$ (offering a much better resolution compared to a confocal image), which – using suitable tuning parameters – hopefully yields RoIs satisfying (R1) and (R3)–(R5). However, strong statistical guarantees such as (R2) do typically not hold. On the other hand, systems of sets satisfying (R2) are often overlapping and thus (possibly highly) redundant, i.e. violate (R3), and furthermore do not satisfy (R5). Our approach is therefore to profit from the strengths of two different approaches, creating a hybrid version that inherits the positive aspects of both ingredients. A theoretical guarantee of property (R1) is very difficult and is not provided by our method. This can still be justified by a liberal choice of the selection method, e.g. in terms of a smaller probability in (R2). However, even with 90% confidence in (R2), our simulations show very good coverage properties of our final segmentation.

3.1. Hybridization

Suppose that the set $\tilde{\mathcal{B}}$ is a (possibly complex and highly redundant) system of sets satisfying (R2). To reduce the complexity (and redundancy) of $\tilde{\mathcal{B}}$, we first neglect all sets that completely contain smaller sets. This might cause a loss of information, but on the other hand we are mostly interested in smaller sets as they contain the highest spatial information. This step yields a system \mathcal{B} of sets obeying (R2).

In the following we describe how the system \mathcal{B} can be hybridized with a segmentation \mathcal{W} (i.e., a system of disjoint connected subsets of $[n] \times [n]$) such that on the one hand, the segmentation property is obeyed, and on the other hand (R2) is kept valid. There is a lot of freedom in choosing the segmentation algorithm, which allows the user to apply any method of choice and hence to generate a system of RoIs consisting of more naturally shaped segments. Possible examples include the famous Watershed segmentation algorithm (see below for a brief description), k -means clustering, or more recent AI-based techniques. Xie et al. (2022) provide a comprehensive review on spatial hotspot detection methodology.

In the hybridization step we try to validate each segment $W \in \mathcal{W}$ using one (or more) of the sets $B \in \mathcal{B}$. Thus let $W \in \mathcal{W}$. If there exists a $B \in \mathcal{B}$ such that $B \subset W$, then W is already valid (in the sense of (R2)). If no such B exists, then we merge W with one of the intersecting sets to generate an enlarged valid segment. This step does, however, cause complications, as the chosen set $\hat{B} \in \mathcal{B}$ might intersect with other segments in \mathcal{W} . This issue is resolved as follows:

1. First, we generate a set of potential *validation sets* $\mathcal{B}_W \subset \mathcal{B}$ such that $W \cap B \neq \emptyset$ for all $B \in \mathcal{B}_W$.
2. If $\mathcal{B}_W = \emptyset$, then W has to be dropped.
3. If $\mathcal{B}_W \neq \emptyset$, we check for each $B \in \mathcal{B}_W$ if $B \in \mathcal{B}_{W'}$ for another $W' \in \mathcal{W}$. This yields a list of candidates for validating W .
4. Out of this list, we choose the one \hat{B} yielding the smallest new (and valid) segment $R := \hat{B} \cup W$.
5. If no such B is found, we merge W with another segment $W' \in \mathcal{W}$, which is again done such that the new resulting segment is as small as possible.

The process described above is repeated iteratively until all segments have been validated or dropped, i.e. until (R2) is satisfied. The final, hybridized segmentation is then given as a set of regions R denoted by $\widehat{\mathcal{ROI}}$. We illustrate this procedure in Figure 3.

The next theorem guarantees that the hybrid selection $\widehat{\mathcal{ROI}}$ provides a valid segmentation in the sense of (R2) and (R3).

Theorem 3.1. *Let $\widehat{\mathcal{ROI}}$ be the regions of interest arising from the above hybridization algorithm of two systems of subsets $\mathcal{B}, \mathcal{W} \subset 2^{[n] \times [n]}$. Then the following holds true:*

1. *Let $\alpha \in (0, 1)$. If the system of sets \mathcal{B} obeys (3.4), then also $\widehat{\mathcal{ROI}}$ does.*
2. *If \mathcal{W} is a segmentation, i.e., if the sets in \mathcal{W} are pairwise disjoint, then also $\widehat{\mathcal{ROI}}$ is a segmentation.*

Proof.

1. It is clear that with $\tilde{\mathcal{B}}$ satisfying (3.4) also any set $\mathcal{B} \subset \tilde{\mathcal{B}}$ satisfies (3.4). The construction of $\widehat{\mathcal{ROI}}$ ensures that it only contains supersets of sets in \mathcal{B} , such that $\widehat{\mathcal{ROI}}$ inherits (3.4).
2. This is clear by construction, as intersecting sets are always merged.

□

Clearly, the question whether (R1) and (R4)–(R5) are also satisfied, depends on the choice of $\tilde{\mathcal{B}}$ and \mathcal{W} . If those are generated suitably, then this will be the case as discussed in the following section.

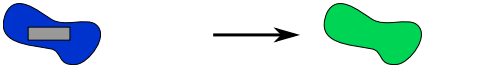
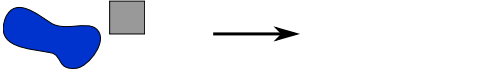
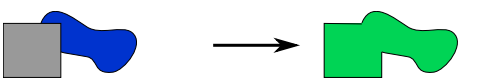


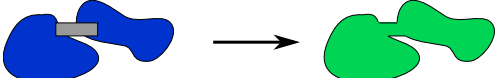
A segment W containing a box B is already valid and kept.	
A segment W intersecting with no box B is dropped.	
A segment W not containing a complete box B is merged with one.	
If there is more than one box B to validate a segment W , the one yielding the smallest resulting segment is chosen.	
If the only possible validating box B intersects with another segment W' , then the resulting region is $R := W \cup B \cup W'$.	
If, in the above situation, another box might validate W , but another W' cannot be validated without merging W and W' , then we optimize this procedure such that the area is as small as possible.	

Figure 3: Illustration of the hybridization algorithm: boxes B (gray), segments W to be validated (blue), final segments (green).

3.2. Practical implementation

In the following we will focus on two specific methods to generate the sets $\tilde{\mathcal{B}}$ and \mathcal{W} . To generate $\tilde{\mathcal{B}}$, we employ the MISCAT procedure introduced in Proksch et al. (2018), which we will briefly describe in the following for convenience (see also Munk et al. (2020a) for a comprehensive review of the MISCAT procedure). We start our segmentation by determining rectangular regions of interest via a multiple testing approach. The rectangular regions will be referred to as boxes, denoted by $B_{\mathbf{x},\mathbf{h}}$. The subscript \mathbf{x} denotes the position of the upper left corner of the box within the grid of pixels, while the subscript $\mathbf{h} = (h_1, h_2)$ denotes the side lengths of the box. For a given \mathbf{h} we consider all $B_{\mathbf{x},\mathbf{h}} \subset \{\mathbf{x}_i \mid \mathbf{i} \in [n] \times [n], \mathbf{i} + \mathbf{h} \in [n] \times [n]\}$ and furthermore we use several different *scales* \mathbf{h} ranging from small to large, so that all together we consider a highly redundant system of boxes that guarantees very good detection properties of the MISCAT method. To test whether a box $B_{\mathbf{x},\mathbf{h}}$ contains markers, we design pairs of functions $\varphi_{\mathbf{x},\mathbf{h}}, \Phi_{\mathbf{x},\mathbf{h}}$ such that

$$\langle f * h, \Phi_{\mathbf{x},\mathbf{h}} \rangle = \langle f, \varphi_{\mathbf{x},\mathbf{h}} \rangle \quad (3.1)$$

with the fluorescence intensity $f = f_N f_p$ where $*$ denotes spatial convolution. Given equation (3.1) and having in mind that $(Y_{\mathbf{i}}^{S,1})_{\mathbf{i} \in [n] \times [n]}$ consists of the most highly resolved measurements available, $\langle (Y_{\mathbf{i}}^{S,1})_{\mathbf{i} \in [n] \times [n]}, \Phi_{\mathbf{x},\mathbf{h}} \rangle$ can serve as a *local test statistic* for testing whether $f|_{B_{\mathbf{x},\mathbf{h}}} \neq 0$. The function pairs $\varphi_{\mathbf{x},\mathbf{h}}, \Phi_{\mathbf{x},\mathbf{h}}$ will in practice be generated by a kernel somewhat similar to Wavelets, such that they form a multiscale system that adapts to the PSF h . This allows optimizing the detection power of MISCAT by fine-tuning the kernel, see Proksch et al. (2018). The local test statistics are then combined by taking the maximum after subtracting a scale-dependent penalization (to ensure equal contribution of the differently sized boxes). This yields a test statistic for a multiple

test over all considered boxes with a controlled family wise error rate as a consequence of Theorem 4 in Proksch et al. (2018). In the latter reference, it is shown in Theorem 1, that quantiles of this maximum (or scan) statistic can be simulated using a suitable Gaussian approximation, which gives then rise to local (taking a suitable scale-penalization into account) critical values $c_{\mathbf{h},\alpha}$. The outcome of this first step is then a set $\tilde{\mathcal{B}}$ of candidate RoIs given by

$$\tilde{\mathcal{B}} = \{B_{\mathbf{x},\mathbf{h}} \mid \langle (Y_{\mathbf{i}}^{\text{S},1})_{\mathbf{i} \in [n] \times [n]}, \Phi_{B_{\mathbf{x},\mathbf{h}}} \rangle \geq c_{\mathbf{h},\alpha}\}.$$

Note, the the resulting candidate RoIs are boxes of different sizes \mathbf{h} . The MISCAT procedure at level α is constructed in such a way that

$$\mathbb{P} \left[\text{There is a pair } (\mathbf{x}, \mathbf{h}) : B_{\mathbf{x},\mathbf{h}} \in \tilde{\mathcal{B}} \mid \text{no markers at all} \right] \leq \alpha. \quad (3.2)$$

Furthermore, as the distribution of the maxima of the statistics $\langle Y^{\text{ST},1}, \Phi_{B_{\mathbf{x},\mathbf{h}}} \rangle$ does not depend on the actual positions of the N markers in the image, we have *subset pivotality*, cf. Westfall and Young (1993). This means that

$$\begin{aligned} \max_{\mathbf{x},\mathbf{h}} \langle (Y_{\mathbf{i}}^{\text{S},1})_{\mathbf{i} \in [n] \times [n]}, \Phi_{B_{\mathbf{x},\mathbf{h}}} \rangle \mid \{\text{no markers present}\} \\ \stackrel{\mathcal{D}}{=} \max_{\mathbf{x},\mathbf{h}} \langle (Y_{\mathbf{i}}^{\text{S},1})_{\mathbf{i} \in [n] \times [n]}, \Phi_{B_{\mathbf{x},\mathbf{h}}} \rangle \mid C, \end{aligned} \quad (3.3)$$

for any $C \in \mathcal{C}_N$, where \mathcal{C}_N is the set of all possible configurations (distributions) of N markers in the image of interest. As a consequence, the FWER control (3.2) for MISCAT implies that with high probability *all selected boxes contain a marker*:

$$\inf_{C \in \mathcal{C}_N} \mathbb{P} \left[f_{|B_{\mathbf{x},\mathbf{h}}} \neq 0 \text{ for all } B_{\mathbf{x},\mathbf{h}} \in \tilde{\mathcal{B}} \mid \text{configuration } C_N \right] \geq 1 - \alpha, \quad (3.4)$$

This is a FWER control over the selected system of boxes in the strong sense, which in general – more precisely without subset pivotality – does not follow from the weaker FWER control (3.2).

For the generation of the segmentation \mathcal{W} , we use here the well-known watershed algorithm, whose name is in reference to a geological watershed, which separates adjacent drainage basins. The algorithm can be applied to grey scale images, which are interpreted as a topographic map, with the brightness of each point representing its height. The algorithm finds the lines that run along the tops of ridges (see Meyer, 1994, for more details).

As a corollary of Theorem 3.1, we obtain for the particular choice of MISCAT at level α and the watershed segmentation \mathcal{W} with any choice of tuning parameter asymptotically

$$\inf_{C \in \mathcal{C}_N} \mathbb{P} \left[\text{Each } \hat{R}_i \in \widehat{\mathcal{ROI}} \text{ contains } \geq 1 \text{ marker} \mid \text{config. } C_N \right] \geq 1 - \alpha.$$

This means that the so obtained hybrid segmentation inherits the strong control of the FWER from the MISCAT procedure.

We illustrate the performance of this hybrid segmentation procedure in Figure 4. The left panel shows simulated data for artificial filamentous structures (resembling among other things the cytoskeleton in cells) generated by the convolution model (2.2) for a STED microscope with different numbers t of excitation pulses. The second panel depicts all boxes selected as significant by the MISCAT procedure color-coded by size. The MISCAT test is able to find a set of significant boxes of various sizes at controlled FWER. However, many of these rectangles are "too large" in the sense that they do not provide spatial information of markers with sufficient accuracy. Moreover, the set $\tilde{\mathcal{B}}$ is highly redundant, which is typical for systems satisfying (R2). The third panel of Figure 4 shows the result of the suggested hybridization, which covers reasonably well the whole structure with non-overlapping significant segments. The fourth panel depicts a histogram of the normalized segment diameter. In total we conclude that all goals (R1)–(R5) are met in general. (R2) and (R3) are ensured by Theorem 3.1 as discussed above independent of the excitation time

$t > 0$. The other requirements clearly depend on the data quality via t . For $t = 1000$ (which is an experimentally reasonable parameter), both (R1) and (R4) are visually satisfied. The shape of the RoIs is mostly determined by the watershed algorithm, and we find that this meets also (R5). The coverage of the structure as well as the number of found segments increases with increased brightness of the image, while the average size of the found significant boxes and hybrid segments decreases.

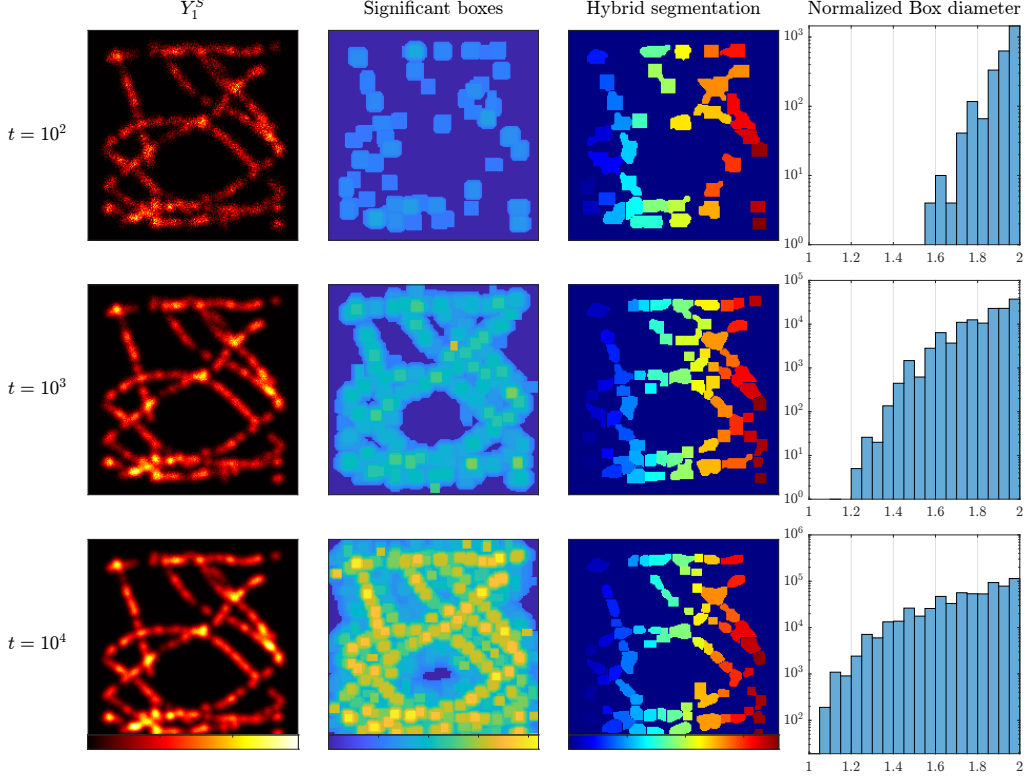


Figure 4: From left to right: 1.) Simulation of filamentous structures: Data sets for different numbers t of excitation light pulses. 2.) MISCAT segmentation where boxes are shown in a color-scale inverse to box area and smaller boxes are drawn on top of larger boxes. 3.) Hybrid segmentation. 4.) Histograms of the segment diameter normalized by the FWHM of the PSF ($\sqrt{|R|}/FWHM$).

4. Statistical molecule counting

In this section we discuss how to estimate the local number of molecules inside a region R from the data. Furthermore, we provide a central limit theorem (CLT) for our estimator, which immediately allows us to construct (asymptotic) confidence intervals quantifying the precision of our counting method. Later on we will apply the methodology presented here to all regions in the previously discussed hybrid segmentation \widehat{ROI} .

For the derivation of our estimator, suppose for a moment that all the N molecules of the specimen are clustered at a single point, this is $\psi(j) = \mathbf{k} \in [n] \times [n]$ for all $1 \leq j \leq N$ with some fixed $\mathbf{k} \in [n] \times [n]$. In this case it follows immediately from the definition that

$$\sum_{\mathbf{i} \in [n] \times [n]} s_l(\mathbf{x}_i) = \sum_{\mathbf{i} \in [n] \times [n]} \sum_{j=1}^N p_j(\mathbf{x}_i) = \sum_{\mathbf{i} \in [n] \times [n]} \sum_{j=1}^N p_j^l \cdot h(\mathbf{x}_i - \mathbf{x}_k)^l.$$

If we now assume that the brightness of all molecules located at the same position is constant (i.e. that the brightness is a function of the location only and not of the individual molecules), we obtain

$$\sum_{\mathbf{i} \in [n] \times [n]} s_l(\mathbf{x}_i) = p^l N \sum_{\mathbf{i} \in [n] \times [n]} h(\mathbf{x}_i - \mathbf{x}_k)^l.$$

In all practically relevant examples, the PSF h is rapidly decaying and can hence be considered as periodic, which justifies the additional assumption that

$$H_l := \sum_{\mathbf{i} \in [n] \times [n]} h(\mathbf{x}_i - \mathbf{x}_k)^l \quad (4.1)$$

is independent of the location $\mathbf{k} \in [n] \times [n]$. Consequently, it holds

$$N = \frac{H_2}{H_1^2} \frac{\left(\sum_{\mathbf{i} \in [n] \times [n]} s_1(\mathbf{x}_i) \right)^2}{\sum_{\mathbf{i} \in [n] \times [n]} s_2(\mathbf{x}_i)}. \quad (4.2)$$

In the situation of Lemma 2.1, the quantities $\mathbf{s}(\mathbf{x}_i)$ can be immediately estimated, as then

$$\mathbf{s}(\mathbf{x}_i) = (\mathbf{T}^{-1}(\mathbf{D}(\mathbf{x}_i)) + O(\gamma(\mathbf{x}_i)^{m_d+1})). \quad (4.3)$$

This leads to a natural plugin estimator for the total number of molecules, where $\mathbf{D}(\mathbf{x}_i)$ is estimated by the relative frequencies of detecting $0, 1, \dots, m_d$ photons at \mathbf{x}_i .

Let us now return to the general situation that we want to estimate

$$N_R = \#\text{markers in } R$$

for some region $R \subset [0, 1]^2$. For this, we pose the following physical assumption:

Assumption 4.1. *The brightness within the region R is constant and the functions H_l defined in (4.1) do not depend on \mathbf{k} .*

This assumption is (approximately) valid for many experimental settings as long as R is not too large, as the brightness depends mostly on local conditions such as temperature, pH value and so on. Under Assumption 4.1 it seems now natural to replace the sum over all locations \mathbf{x}_i in (4.2) by the sum over all $\mathbf{x}_i \in R_\varepsilon$ with a slightly enlarged segment $R_\varepsilon = \{x \in [0, 1] \mid \text{dist}(x, R) \leq \varepsilon\}$. The rationale behind is that the rapid decay of the PSF h ensures that molecules inside R will only or at least mostly contribute to those $\mathbf{x}_i \in R$. In practice we choose ε of the order of the FWHM and enlarge only as long as R_ε does not intersect with any other enlarged segment. Let us introduce $\mathcal{I}_{R_\varepsilon} := \{\mathbf{i} \in [n] \times [n] \mid \mathbf{x}_i \in R_\varepsilon\}$. Then the above considerations give rise to the plugin estimator

$$\hat{N}_R = \frac{H_2}{H_1^2} \frac{\left(\sum_{\mathbf{i} \in \mathcal{I}_{R_\varepsilon}} \hat{s}_1(\mathbf{x}_i) \right)^2}{\sum_{\mathbf{i} \in \mathcal{I}_{R_\varepsilon}} \hat{s}_2(\mathbf{x}_i)} \quad \text{with} \quad \hat{\mathbf{s}}(\mathbf{x}_i) = \mathbf{T}^{-1} \mathbf{Y}_i^C / t.$$

Note that the inversion of \mathbf{T} might introduce uncertainties (and actually does, cf. Figure 5 in our numerical simulations), and as the noise level of $\hat{s}_k(\mathbf{x}_i)$ increases geometrically with k in view of the f_p^k -dependency, we decided to use only $\hat{s}_1(\mathbf{x}_i)$ and $\hat{s}_2(\mathbf{x}_i)$ to infer on N_R . Nevertheless, it is in principle possible to improve the estimate for N_R based on higher order contributions $s_k(\mathbf{x}_i)$, $k \geq 2$ along the above considerations.

The following central limit theorem for the estimator \hat{N}_R is based on asymptotics for $t \rightarrow \infty$ subject to $m_d = m_d(t) \rightarrow \infty$. Given these asymptotic considerations, we will assume that t is large enough such that the model bias (2.6) is irrelevant. Since the influence of the size of m_d is of practical interest, finite sample bounds of Berry-Esseen type with respect to t as well as m_d are additionally provided. Denote by $\Pi_{(k_1, \dots, k_l)}^d : \mathbb{R}^d \rightarrow \mathbb{R}^l$ the projection of a vector in \mathbb{R}^d onto the vector of its coordinates k_1, \dots, k_l .

Theorem 4.2. Let $R \subset [0, 1]^2$ and let $m_d = m_d(t) \rightarrow \infty$, such that $m_d \leq 5 \log(t)$. Suppose that the region R contains at least one fluorescent marker, that Assumption 4.1 is satisfied, and that any marker in R has individual brightness smaller than 0.5 (see Remark 4.3 (v)). Let

$$\Sigma_{\mathbf{D}}(\mathbf{x}_i) = \left(\begin{array}{cc} D_j(\mathbf{x}_i)(1 - D_j(\mathbf{x}_i)) & j = k \\ -D_j(\mathbf{x}_i)D_k(\mathbf{x}_i) & j \neq k \end{array} \right)_{j,k=1}^{m_d},$$

and consider an arbitrary but fixed ordering $\mathbf{x}_{i_1}, \dots, \mathbf{x}_{i_{|R|}}$ of the points $\mathbf{x}_i \in R$. Further, define the matrix Σ_R by

$$\Sigma_R := \begin{pmatrix} \Sigma_{\mathbf{D}}(\mathbf{x}_{i_1}) & \mathbf{0} & \mathbf{0} & \mathbf{0} \\ \mathbf{0} & \Sigma_{\mathbf{D}}(\mathbf{x}_{i_2}) & \mathbf{0} & \mathbf{0} \\ \mathbf{0} & \mathbf{0} & \ddots & \mathbf{0} \\ \mathbf{0} & \mathbf{0} & \mathbf{0} & \Sigma_{\mathbf{D}}(\mathbf{x}_{i_{|R|}}) \end{pmatrix} \in \mathbb{R}^{|R|m_d \times |R|m_d}$$

and let

$$\Psi : \begin{cases} \mathbb{R}^{|R|m_d|} \rightarrow \mathbb{R} \\ \mathbf{y} \mapsto \frac{H_2}{H_1^2} \cdot \frac{\langle \mathbf{1}_{m_d|R|}, (\Pi_1^{m_d} \mathbf{T}^{-1}(y_{j m_d+1}, \dots, y_{(j+1)m_d})^T)_{j=1, \dots, |R|} \rangle^2}{\langle \mathbf{1}_{m_d|R|}, (\Pi_2^{m_d} \mathbf{T}^{-1}(y_{j m_d+1}, \dots, y_{(j+1)m_d})^T)_{j=1, \dots, |R|} \rangle} \end{cases}.$$

Assume that the Hessian matrix of Ψ , Hess_{Ψ} , exists and is bounded in a neighbourhood of \mathcal{D} , and that

$$\sigma_R^2 = \nabla \Psi(\mathcal{D})^T \Sigma_R \nabla \Psi(\mathcal{D}) > 0, \quad (4.4)$$

where $\mathcal{D} = (\mathbf{D}(\mathbf{x}_{i_j}))_{j=1, \dots, |R|}$. Let Z be a random variable following a centered normal distribution with variance σ_R^2 . If t is sufficiently large, there exists a constant $C > 0$ such that

$$\sup_{s \in \mathbb{R}} \left| \mathbb{P} \left(\sqrt{t} (\hat{N}_R - N_R) \leq s \right) - \mathbb{P} \left(Z \leq s \right) \right| \leq C \frac{\log(t)^{\frac{2}{3}}}{t^{\frac{1}{6}}}, \quad \text{as } t \rightarrow \infty. \quad (4.5)$$

Remark 4.3.

(i) In particular, the above theorem ensures that

$$\sqrt{t} (\hat{N}_R - N_R) \xrightarrow{\mathcal{D}} \mathcal{N}(0, \sigma_R^2), \quad \text{as } t \rightarrow \infty.$$

- (ii) Recall that the asymptotic considerations are with respect to the number t of laser pulses. As t tends to infinity, the number of pixels remains fixed. Therefore, the collection of regions R considered does not change asymptotically and contains only finitely many elements. Therefore, naturally, (4.5) holds uniformly in R .
- (iii) We let $m_d \rightarrow \infty$ as $t \rightarrow \infty$, as for a fixed number m_d the model bias (2.5) may otherwise asymptotically dominate the quantity $\sqrt{t}(\hat{N}_R - N_R)$. The upper bound on the speed of convergence of m_d is needed in the proof, as with m_d the number of events of the multinomial distribution tends to infinity. However, this restriction is irrelevant in practice, where the number of detectors that can be realized is limited.
- (iv) In this work, the focus is on the estimation of local numbers of molecules, N_R . However, similar to (4.2), we immediately obtain an expression for p_R , the brightness in a region R , as

$$p_R = \frac{H_1}{H_2} \frac{\sum_{\mathbf{i} \in \mathcal{I}_R} s_2(\mathbf{x}_i)}{\sum_{\mathbf{i} \in \mathcal{I}_R} s_1(\mathbf{x}_i)},$$

giving rise to a plug-in estimator \hat{p}_R . The theoretical properties of \hat{p}_R can be analyzed with the same techniques as applied in the analysis of \hat{N}_R .

- (v) We assumed that any marker in R has individual brightness smaller than 0.5. This assumption is needed for technical reasons but it is not restrictive, as typical brightness values are of the order of 0.02, as also used in our simulations. A brightness of 0.5 would entail that a marker emits a photon on average once every two pulses, which is unrealistic.
- (vi) Given that $m_d \rightarrow \infty$, the model bias vanishes asymptotically. Our numerical simulations show that as few as 6 detectors suffice to deal with local numbers of molecules of about 100 (see Figure 8). The experimental setup we used (as shown in Figure 1) exploits $m_d = 4$ detectors, and we find from Figure 8 that it is expected to be accurate to treat local molecule numbers of round 30 – 40.

Theorem 4.2 gives rise to asymptotic confidence intervals for N_R

$$\left[\hat{N}_R - \frac{\hat{\sigma}_R}{\sqrt{t}}, \hat{N}_R + \frac{\hat{\sigma}_R}{\sqrt{t}} \right],$$

where $\hat{\sigma}_R$ is the plug in estimator for the asymptotic standard deviation σ_R defined in (4.4), that is, $\hat{\sigma}_R = \nabla \Psi(\hat{\mathcal{D}})^T \Sigma_R \nabla \Psi(\hat{\mathcal{D}})$, with $\hat{\mathcal{D}} = 1/t \cdot (\mathbf{Y}_i^C)_{i \in R}$.

5. Numerical study

In this section we will investigate the finite sample properties of our estimation procedure and the overall algorithm. The complete MATLAB[®] code including all examples discussed in the manuscript at hand is available under

https://github.com/jkfindeisen/antibunching_microscopy_analysis_2022.

As a first step, we assumed a certain number of independent and identically behaving molecules with a fixed brightness p to be located all at the same position and to be imaged with the antibunching microscope operating only on confocal mode. The recording of the molecule sample is performed by scanning on a square-lattice like grid relative to the molecules' position and the grid spacing is here defined relative to the resolution of the microscope, i.e. with a FWHM of the PSF given in scanning grid pixel sizes. For a single cluster, segmentation of the data was omitted and the whole measurement area was assumed to belong to the single segment representing the molecule cluster. In Figure 5 we depict histograms of the empirical distributions of $S_l := \sum_{\mathbf{i} \in [n] \times [n]} s_l(\mathbf{x}_i)$ together with the theoretical expectations of S_l . It can be seen that for typical experimental conditions, the first two orders of S_l are reasonably well distributed around their expectations and can be used for retrieving the number and brightness of the molecules. For higher orders, systematic deviations are visible in the distributions of S_l , most probably a side effect of the ill-conditioned inversion of \mathbf{T} under these circumstances.

This first simulation shows that it is possible to estimate the number of molecules in a single, isolated cluster from S_1 and S_2 . This is further illustrated in Figure 6, where we investigate the final estimator for the total number of molecules N (and the corresponding one for the common brightness p as discussed in Remark 4.3(iv)) in a similar setting. Again we use a single cluster with $N = 10$ molecules with common brightness $p = 0.02$ and omit the segmentation step by assuming that the whole measurement area was assumed to belong to the single segment representing the molecule cluster. Repetition of the simulation results in distributions for \hat{N} and \hat{p} , which are depicted as histograms. It should be noted that the estimated molecule numbers and brightnesses are correlated and the joint distribution is concentrated along a hyperbola in the number-brightness plane (see Fig. 6c), i.e. the product of the molecule number and its brightness is quite well estimated compared to the knowledge about the single factors. For larger numbers of illumination pulses the distributions of the estimated numbers and brightnesses becomes more concentrated, more symmetric and less biased, indicating that the employed estimators converge to the true underlying parameters. The precision is mainly limited by the number of repetitions, i.e. light pulses, that the sample can be illuminated with at every scan position. A few thousand

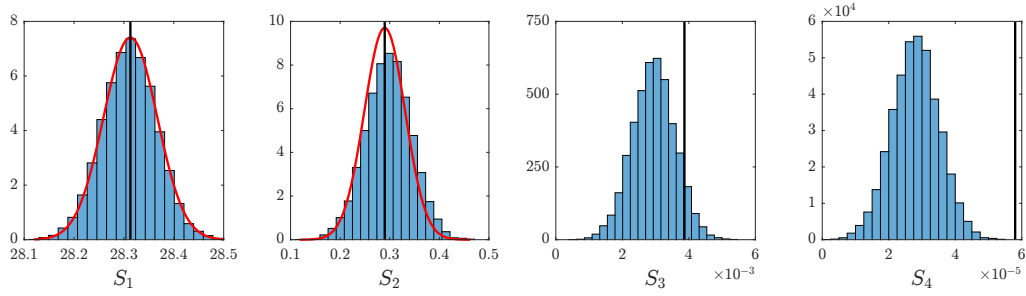


Figure 5: Estimation of $S_l := \sum_{\mathbf{i} \in [n] \times [n]} s_l(\mathbf{x}_i)$ for simulations of single, isolated cluster of $N = 20$ molecules with brightness $p = 0.02$ and a Gaussian PSF of FWHM=4px and $t = 10^4$ pulses per pixel. Histograms of estimated S_i for many repetitions. Vertical lines (black) present the true mean values. Red curves represent normal distributions with true variances around the true means.

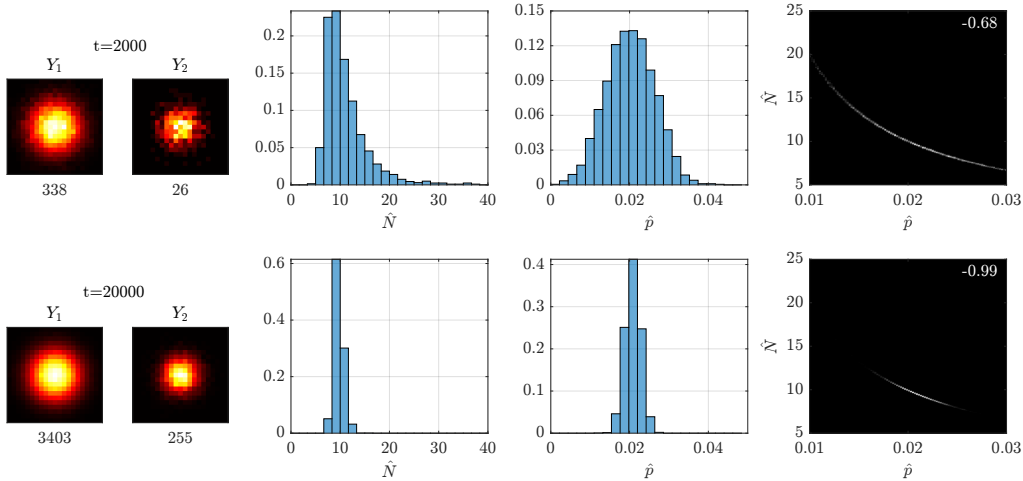


Figure 6: Histograms of estimated N and p for simulations of single, isolated cluster of $N = 10$ molecules with brightness $p = 0.02$ and a Gaussian PSF of FWHM=4px and $t = 10^3$ and $t = 10^4$ pulses per pixel, respectively.

excitation pulses per scan position have been reported to be possible without significant observable photobleaching of the molecules.

To study the influence of boundary effects, i.e. molecules residing close to the boundary of an image segment, we simulated two clusters of molecules with a defined distance that is on the order of the FWHM of the PSF. In that way the images of the two clusters are partly overlapping. Two segments were created such that they fully covered the whole simulated image space and the border between the two segments was localized in the middle between the clusters. The analysis in each segment will be compromised by photons that are located in the respective other segment. The results depicted in Figure 7 show that for a reasonable cluster distance (of approximately the FWHM of the PSF) the systematic boundary effects tend to become relatively small. It should be noted that our hybrid segmentation naturally tends to avoid large amounts of signal close to segment borders.

Another source of systematic bias are very dense accumulations of molecules. Therefore, we performed simulations in which we increased the number of detectors. We found that the range of molecules that can be estimated without visible bias strongly increases already for a number of detectors that is increased only moderately. Four parallel detectors, which are currently used experimentally, allow to count up to 50 molecules per diffraction limited sample volume without

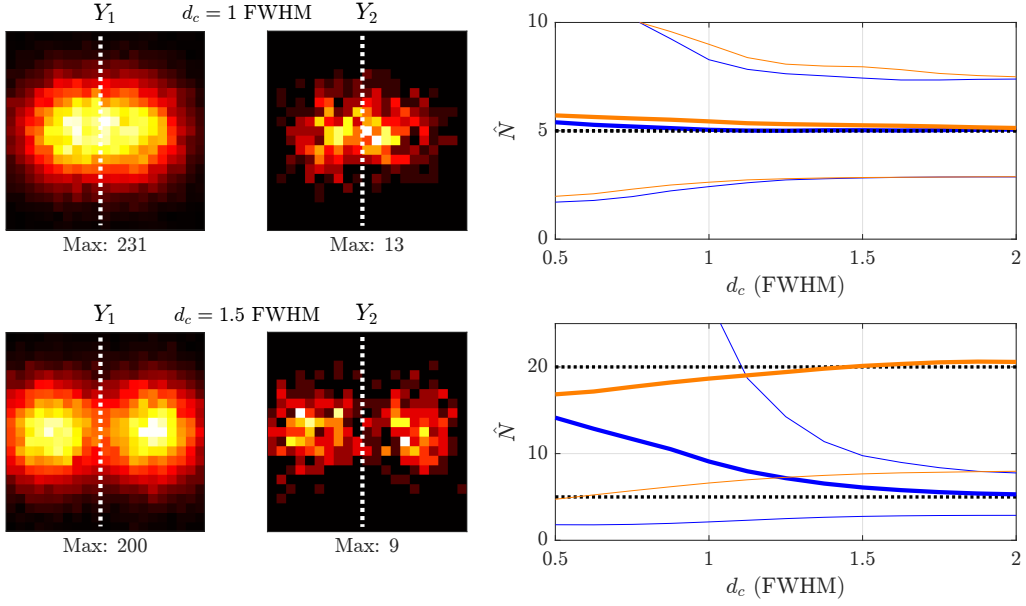


Figure 7: Estimated N for simulations of two clusters of molecules with a defined distance d_c (given in multiples of the FWHM) with brightness $p = 0.02$, $t = 3000$ and a Gaussian PSF of FWHM=4px. (left) Example images of two clusters with five molecules each. Dotted white line represents the segment border. (right) Mean estimated number of molecules for each cluster and mean lower and upper bounds of the confidence intervals (thin lines) in dependence of the distance d_c between the clusters. Black dotted line represents the true number of molecules in each cluster. Top: two clusters with $N_1 = N_2 = 5$ and bottom: $N_1 = 5, N_2 = 20$.

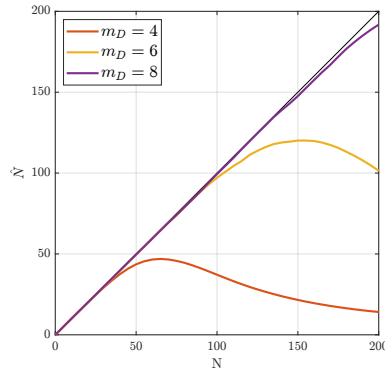


Figure 8: Median of estimated number of molecules for a simulation of a single cluster ($p = 0.02$, $t = 2 \cdot 10^4$) in dependence of the number of detectors used m_d . The visible bias is strongly reduced for larger m_d . All internal orders equal m_d . Graphs are slightly smoothed.

large bias with our method. With eight parallel detectors this limit could be lifted to approximately 200, cf. the left panel in Figure 8.

The overall performance of our algorithm is tested in a simulated arrangement of markers consisting of several clusters of molecules with varying brightness, cf. Figure 2. It shows that the estimation of the local number of molecules is accurate in all segments, and that the FWER control (3.4) is in fact kept. It must be said that some of the constructed confidence intervals seem to be rather large (indicating a small estimated value \hat{p} in that region), which is, however, unavoidable when asking for strong error controls such as (3.4). In addition, in Figure 2 the true

values of N_R are located on the boundary of the confidence intervals in multiple cases, indicating that any method with smaller confidence intervals, which are centered at \hat{N}_R , would be susceptible to violations of (1.1).

6. Counting fluorophores in a DNA origami measurement

To establish the validity of the suggested confidence intervals on real data we used DNA origami sheets, which is an artificial structure that allows to attach a relatively well defined number of molecules at defined positions within a diffraction-limited volume (Schmied et al., 2012). The designed DNA origami sheet contained up to 24 fluorophores arranged in two lines of up to 12 fluorophore binding sites and the distance between the two lines was ~ 70 nm, which is not resolvable in confocal mode. Due to imperfections in the folding efficiency of DNA, the expected number of fluorophores per DNA origami was only ~ 19 (Ta et al., 2015). Confocal microscopy cannot spatially resolve the single lines of fluorophores, but it allows to obtain a sufficient statistic on one and two photon detection events. A subsequent STED recording with improved lateral resolution (fivefold over confocal microscopy) resolved the molecular distribution within a single DNA origami sheet. Further experimental details are laid out in Ta et al. (2015). Here, we re-analyzed the recorded data to yield estimates and confidence intervals on the number of fluorophores in either resolved DNA origami sheets or even single lines in these sheets (see Fig. 9). The division of the data into suitable segments using our hybrid MISCAT and watershed segmentation approach was performed on the high resolution STED data, while the molecular number and brightness was estimated from the less well resolved but much brighter one- and two-photon confocal images. Before counting, the background intensity is estimated by a smoothing procedure from the data and then included in our refined model. The result is a segmentation map of the image area shown in Fig. 9b where an estimated number of molecules as well as a confidence interval on the number of molecules is assigned to each segment. As expected the estimated number of molecules is always within the calculated confidence bounds. The width of the confidence bounds (K) is approximately as large as the estimated number of molecules.

7. Discussion and outlook

7.1. Summary

In this work, a comprehensive physical and statistical modeling of the coincidence photon statistics encountered in antibunching microscopy has been conducted. The coincidence signals recorded from parallel detectors in a high-resolution fluorescence microscope intricately depend on the number of fluorescent molecules at a specific location as well as their brightness. Under the mild assumption that molecules locally exhibit the same brightness, and under neglecting all background contributions, a rigorous statistical model of the problem of estimating the number of molecules within small regions of the sample has been developed. Based on this an estimation procedure of the number of molecules was presented and was shown to converge to the true molecule counts for sufficiently long measurement times. Furthermore, confidence intervals for the local number of molecules have been constructed. The estimation procedure requires to choose regions of the sample in which molecule numbers are to be estimated. A hybrid-segmentation has been introduced, which combines a natural segmentation approach with guarantees that all segments contain molecules with high probability. In a numerical study, the convergence of the estimator has been affirmed. With increasing number t of excitation pulses the obtained segment sizes as well as the size of the confidence intervals have been shown to shrink.

7.2. Future work

In previous works the number of molecules (as well as their brightness) was estimated as a continuous density from a global fit of the data with a coincidence statistics model up to second order

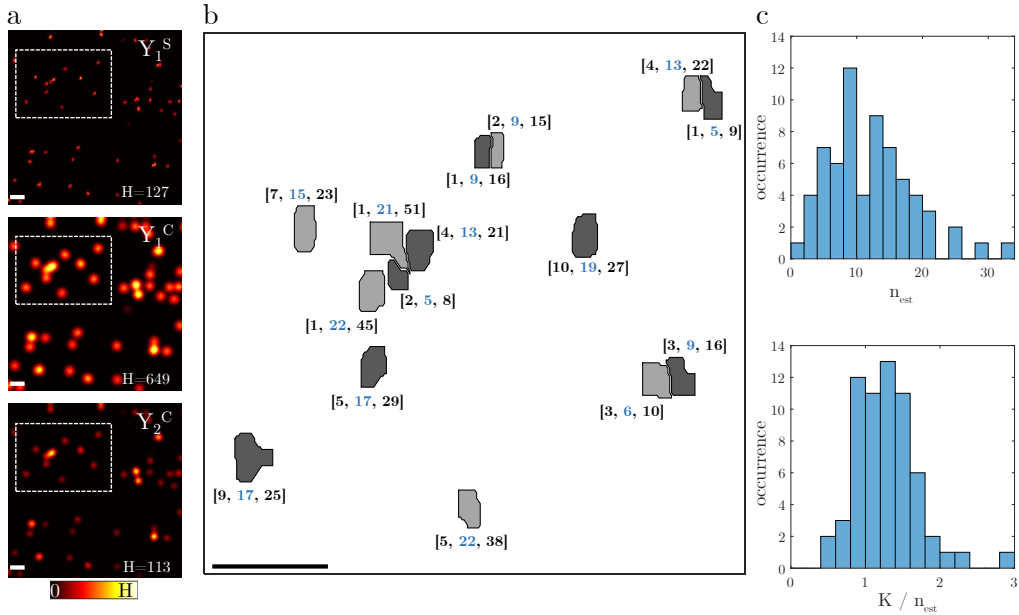


Figure 9: Application to recordings of DNA origami sheet structures labelled with ATTO 647N molecules (for experimental details see (Ta et al., 2015)). The structures were immobilized at a low concentration on a glass surface and measured with confocal and STED microscopy. Each DNA origami can accommodate up to 24 fluorophores (12 in a line). **a** STED (top) and confocal (number of pulses per pixel $t=2170$, pixel size 10 nm) one-photon (center) and two-photon (bottom) detection images. **b** Segmentation, estimated number of fluorophores in each segment and confidence intervals for the data in the dotted rectangle. **c** Histogram of estimated number of fluorophores in each segment of the recorded data (top) and histogram of the width of the confidence interval (K) divided by the estimated number of fluorophores (bottom). Scale bars, 500 nm.

(Ta et al., 2015). The model presented here includes arbitrarily high photon coincidence orders. In this work only the lowest two orders of $\hat{s}_k(\mathbf{x}_i)$ have been used in the estimation of the local number of molecules. The optimal choice of the used number of orders depends on the accuracy of the estimation of each \hat{s}_k and may be subject to further studies. An important issue here is the quality of the available data (i.e. the possible number of excitation pulses t), as otherwise the higher order photon coincidences will not be able to provide additional information.

Segmentation-based estimation of local molecular counts was essential for the generation of confidence information. The importance of choosing an appropriate sample segmentation which provides statistically sound guarantees (see Theorem 3.1) for generating useful confidence information is a key finding of this work. A very large number of localized segments would result in overly large confidence intervals (due to multiplicity), while a small number of extended segments would not result in meaningful local information. A balanced approach as suggested in this work results in useful molecule counting information. A multitude of different segmentations are imaginable but the hybrid segmentation used in this work appears to be working reasonably well. Further work might deliver more insights into how segmentations of the sample can maximize the usefulness of the counting information in these cases.

The enlarged segments used for estimation are in principle required to contain all the collected fluorescence from all molecules within the segment and none from molecules outside the segment (segments should contain a molecule-free border with a width of at least the FWHM of the PSF). Clearly, this is not always the case in practice, and is often difficult to achieve in densely labelled samples unless one restricts oneself to rather large segments, which would not result in

useful local information. This will in general result in an uncontrollable bias in the molecule number estimation. In the case of multiple closely spaced segments, lost photon contributions from molecules within a segment can be partially compensated by contributions from molecules in adjacent segments. In our examples the estimated confidence intervals were not compromised. A further careful analysis of segment border effects might result in additional contributions to the confidence interval sizes.

The analysis performed in this study also assumed that molecules remain intact during the whole measurement. Indeed, in every microscopy experiment, fluorophores will eventually lose their ability to fluoresce (photobleach). To minimize estimation biases, we restricted the duration of the experiment to the characteristic time that will leave a strong majority of fluorophores intact. Should, nevertheless, some molecules photobleach during an experiment, we expect the number estimation to effectively approximate the mean number of unbleached molecules during the measurement. Photobleaching could be included in a more refined statistical model.

As discussed in the simulations, a too large number of molecules (or more precisely a too large product of local number of molecules and their brightness) in comparison to the number m_d of detectors used yields a systematic under-estimation of the number of molecules. This is due to the fact the bias introduced by the model from Theorem 2.1 is no longer negligible. Our current experimental setup shown in Figure 1 using four detectors is able to count approximately 50 molecules at a single diffraction limited spot accurately. Increasing the number of detectors modestly would increase this limit significantly as shown in Figure 8. Further advances in detector technology currently being invented (being able to count single photons without significant dead times and therefore not limiting the observable coincidence photon order) are expected to diminish if not solve the problem completely while at the same time simplifying the microscope setup further.

All given examples in this work have been executed in two dimensions only, which corresponds to an often used imaging mode in scanning microscopy. However, the extension to 3D is straightforward and does not require any particular effort.

A. Proofs

Proof of Theorem 2.1

Lemma A.1. *In the setting of Theorem 2.1, there exists a linear map A and a non-linear transformation g such that $\mathbf{T} = A \circ g$.*

Proof of Lemma A.1. Due to superposition and independence of the markers, for each position \mathbf{x} the random variable that returns the number of photons emitted after one excitation pulse follows a discrete probability distribution of a sum of independent Bernoulli trials that are not necessarily identically distributed. This distribution is called *Poisson binomial distribution* (Tang and Tang, 2019). The probability that exactly k photons are emitted at scan position \mathbf{x} in one experiment is denoted by $Q'_k(\mathbf{x})$, which is given by

$$Q'_0(\mathbf{x}) = \prod_{j=1}^N (1 - p_j(\mathbf{x})),$$

$$Q'_k(\mathbf{x}) = \sum_{1 \leq i_1 < \dots < i_k \leq N} \prod_{j=1}^k p_{i_j}(\mathbf{x}) \prod_{j \neq i_1, \dots, i_k} (1 - p_j(\mathbf{x})),$$

for $k \in \{1, \dots, N\}$. Note, that for $k > 1$ $Q'_k(\mathbf{x})$ requires the different photons to originate from different markers. In practice, we do not have direct empirical access to the probabilities Q'_k . To see this, suppose for instance that $m_d = 4$ as in Figure 1, and that 2 photons were emitted. If the beam splitters in our experimental setup distribute the incoming photons equally likely in each direction, then after the first beam splitter with probability 50%, the photons have been separated and will arrive at different detectors. On the other hand, in 50% of the cases, both photons have been sent in the same direction and will arrive together at the next beam splitting. Continuing this

argument, it follows that in 75% of all cases, the two photons are sent towards different detectors, whereas in 25% of all cases, the two photons are sent towards a single detector, which cannot differentiate the number of incident photons. Therefore, with

$$D_i(\mathbf{x}) := \mathbb{P}(i \text{ active detectors at } \mathbf{x} \text{ in one experiment}),$$

the probability $Q'_2(\mathbf{x})$ distributes with weight 1/4 to the probability $D_1(\mathbf{x})$ to observe a single active detector, and with weight 3/4 to the probability $D_2(\mathbf{x})$ to observe exactly two active detectors. The probabilities D_i can be computed in terms of the Q'_i 's as

$$\begin{aligned} D_i(\mathbf{x}) &= \sum_{j=i}^N \mathbb{P}(i \text{ active detectors} \mid j \text{ photons}) \times \mathbb{P}(j \text{ photons}) \\ &= \sum_{j=i}^N \mathbb{P}(i \text{ active detectors} \mid j \text{ photons}) Q'_j(\mathbf{x}). \end{aligned}$$

Given that j photons are emitted, there are in total m_d^j ways to distribute those onto m_d detectors. The total number of outcomes in which $0 \leq i \leq m_d$ detectors are activated is given by the product of the number of possibilities to distribute j photons onto one specific selection of i detectors and the number of different choices of i out of m_d detectors. The first factor is given by $S(j, i) \times i!$, where $S(j, i)$ denote the Stirling numbers of the second kind¹. The second factor is given by the binomial coefficient $\binom{m_d}{i}$. Since the emitted photons are distributed with equal probability onto m_d detectors, we obtain

$$\mathbb{P}(i \text{ active det.} \mid j \text{ photons}) = \frac{S(j, i) \cdot i! \cdot \binom{m_d}{i}}{m_d^j} = \frac{S(j, i)(m_d - i)!}{(m_d - i)!m_d^{j-1}} =: w_{i,j}.$$

This yields

$$D_i(\mathbf{x}) = \sum_{j=i}^N Q'_j(\mathbf{x}) w_{i,j},$$

which yields that $D_0(\mathbf{x}) = Q'_0(\mathbf{x})$, meaning that whenever at least one photon is emitted, at least one detector will be active. Moreover, the contribution of summands for large values of j , $j > m_d$ say, are negligible. Hence, we write

$$D_i(\mathbf{x}) = \sum_{j=i}^{m_d} Q'_j(\mathbf{x}) w_{i,j} + \sum_{j=m_d+1}^N Q'_j(\mathbf{x}) w_{i,j}.$$

Let $\mathbf{Q}(\mathbf{x}) = (Q'_1(\mathbf{x}), \dots, Q'_{m_d}(\mathbf{x}))^T$ denote the vector of the first m_d probabilities Q'_k and let $\mathbf{D}(\mathbf{x}) = (D_1(\mathbf{x}), \dots, D_{m_d}(\mathbf{x}))^T$. Then, for $i > 0$, we obtain the following connection between \mathbf{D} and \mathbf{Q}

$$\mathbf{D}(\mathbf{x}) = A\mathbf{Q}(\mathbf{x}) + \sum_{j=m_d+1}^N Q'_j(\mathbf{x}) \mathbf{w}_j, \quad (\text{A.1})$$

with

$$A = (w_{p,q} I\{p \leq q\})_{p,q=1}^{m_d}$$

and $\mathbf{w}_j = (w_{1,j}, \dots, w_{N,j})$. The triangular matrix A satisfies $\det(A) = \prod_{l=1}^{m_d} w_{l,l} > 0$ and therefore, the matrix A is invertible.

¹The Stirling number $S(j, i)$ is the number of ways to partition a set of j objects into i non-empty subsets.

Next, we derive representations of the probabilities Q'_k in terms of

$$\begin{aligned} s_k(\mathbf{x}) &:= \sum_{i=1}^N \mathbf{p}_i(\mathbf{x})^k, \quad k \in \mathbb{N}, \\ S_k(\mathbf{x}) &:= \sum_{\substack{i_1, \dots, i_k \in \{1, \dots, N\} \\ i_1 \neq \dots \neq i_k}} \mathbf{p}_{i_1}(\mathbf{x}) \cdot \dots \cdot \mathbf{p}_{i_k}(\mathbf{x}), \quad k \in \mathbb{N}_0, \end{aligned}$$

which give rise to

$$Q'_k(\mathbf{x}) = \frac{1}{k!} \sum_{j=0}^{N-k} \frac{(-1)^j}{j!} S_{j+k}(\mathbf{x}), \quad 0 \leq k \leq m_d. \quad (\text{A.2})$$

Here, the factors $1/k!$ and $1/j!$ arise from the number of possible orderings when replacing $\{1 \leq i_1 < \dots < i_k \leq N\}$ with $\{i_1, \dots, i_k \mid i_1 \neq \dots \neq i_k\}$, respectively. Note that the iterated sums $S_k(\mathbf{x})$ can be computed recursively, requiring knowledge of the $s_k(\mathbf{x})$ only, by the formula

$$\begin{aligned} S_0 &= 1, \\ S_k &= \sum_{j=1}^k (-1)^{j+1} \frac{(k-1)!}{(k-j)!} s_j S_{k-j}, \end{aligned} \quad (\text{A.3})$$

Define the nonlinear transformation $g: \mathbb{R}^{m_d} \rightarrow \mathbb{R}^{m_d}$ by

$$g(s_1(\mathbf{x}), \dots, s_{m_d}(\mathbf{x})) = \left(\frac{1}{k!} \sum_{j=0}^{m_d-k} \frac{(-1)^j}{j!} S_{j+k}(\mathbf{x}) \right)_{1 \leq k \leq m_d} =: (\tilde{Q}_k(\mathbf{x}))_{1 \leq k \leq m_d},$$

with $S_j(\mathbf{x})$ as in (A.3). Furthermore, we find

$$\begin{aligned} A(g(\mathbf{s}(\mathbf{x}))) &= A\mathbf{Q}(\mathbf{x}) - A \left(\frac{1}{k!} \sum_{j=m_d-k+1}^{N-k} \frac{(-1)^j}{j!} S_{j+k}(\mathbf{x}) \right)_{1 \leq k \leq m_d} \\ &= \mathbf{D}(\mathbf{x}) - A \left(\frac{1}{k!} \sum_{j=m_d-k+1}^{N-k} \frac{(-1)^j}{j!} S_{j+k}(\mathbf{x}) \right)_{1 \leq k \leq m_d} - \sum_{j=m_d+1}^N Q'_j(\mathbf{x}) \mathbf{w}_j. \end{aligned}$$

Since

$$\begin{aligned} \left\| \sum_{j=m_d+1}^N Q'_j(\mathbf{x}) \mathbf{w}_j \right\|_2 &\leq \sum_{j=m_d+1}^N \gamma^j \|\mathbf{w}_j\|_2 \leq \sqrt{m_d} \sum_{j=m_d+1}^N \gamma^j, \\ &= \sqrt{m_d} \frac{1 - \gamma^{N-m_d}}{1 - \gamma} \cdot \gamma^{m_d+1}, \end{aligned}$$

$\|A\|_2 \leq 1$ and, for any k ,

$$\frac{1}{k!} \sum_{j=m_d-k+1}^{N-k} \frac{(-1)^j}{j!} S_{j+k}(\mathbf{x}) \leq \frac{e-1}{k!} \gamma^{m_d+1}$$

the claim of Lemma A.1 now follows. \square

To conclude the proof of Theorem 2.1, it remains to show that the map g is invertible. Given $\tilde{Q}_k, k = 1, \dots, m_d$, the quantities S_1, \dots, S_{m_d} can be recovered as follows. Starting with $k = m_d$, we obtain

$$\tilde{Q}_{m_d}(\mathbf{x}) \cdot m_d! = S_{m_d}(\mathbf{x}).$$

Next, for $k = m_d - 1$, we obtain

$$\tilde{Q}_{m_d-1}(\mathbf{x}) = \frac{1}{(m_d - 1)!} \cdot (S_{m_d}(\mathbf{x}) + S_{m_d-1}(\mathbf{x})),$$

yielding

$$(m_d - 1)! \cdot \tilde{Q}_{m_d-1}(\mathbf{x}) - S_{m_d}(\mathbf{x}) = S_{m_d-1}(\mathbf{x}).$$

Successively, S_{m_d-2}, \dots, S_1 can be recovered in the same fashion. Given S_1, \dots, S_{m_d} , we can compute s_1, \dots, s_{m_d} successively as well. Starting with $k = 1$, we find $S_1 = s_1 \cdot S_0 = s_1$. Next, for $k = 2$, we find $S_2 = s_1 S_1 - s_2 S_0$, which gives $s_2 = s_1^2 - S_2$. One by one, s_3, \dots, s_{m_d} can be recovered. \square

Proof of Theorem 4.2

We will give the proof for the case of $|R| = 1$. While it immediately extends to the case $|R| > 1$, it provides a substantial ease of notation. In the proof of Lemma 2.1, the matrix A and the function g have been defined for the case $N > m_d$ as this is the relevant case in practice. However, for our asymptotic considerations, we need to extend these quantities to the case of $N \leq m_d$. Since these definitions are somewhat artificial and are only relevant within this proof, we will denote them as A_t and g_t , respectively. First, we define the matrix A_t . To this end, let $a_{p,q} = 0$, if $q < p$ or if $p < q$ and $q > N$ and let $a_{p,q} = w_{p,q}$ else. Then $A_t = (a_{p,q})_{p,q=1,\dots,m_d}$. With this definition, the matrix A_t is an upper triangular matrix with positive diagonal elements and block structure

$$A_t = \begin{pmatrix} A_1 & A_2 \\ A_3 & A_4 \end{pmatrix}, \quad (\text{A.4})$$

where $A_1 \in \mathbb{R}^{N \times N}$ and $A_4 \in \mathbb{R}^{(m_d-N) \times (m_d-N)}$ are upper triangular matrices with positive diagonal elements, $A_2 = \mathbf{0} \in \mathbb{R}^{N \times (m_d-N)}$ and $A_3 = \mathbf{0} \in \mathbb{R}^{(m_d-N) \times N}$. Therefore, A_t^{-1} exists and has the same block structure. Now, in order to define the function g_t , let

$$b_{i,j} = \begin{cases} \frac{1}{i!} \frac{(-1)^{j-i}}{(j-i)!} & i = j \text{ or } j > i \text{ and } j \leq N \\ 0 & \text{else} \end{cases}.$$

Then, the matrix $B := (b_{i,j})_{i,j=1,\dots,m_d}$ has the same structure as the matrix A_t in (A.4). In particular, B is invertible with $B^{-1} = (\beta_{i,j})_{i,j=1,\dots,m_d}$. Define

$$g_t(s_1(\mathbf{x}), \dots, s_{m_d}(\mathbf{x})) = B \cdot (S_1(\mathbf{x}), \dots, S_{m_d}(\mathbf{x}))^T,$$

where the relation between the s_k 's and the S_k 's is given in (A.3). Notice that $A_t = A$ and $g_t = g$ if $N > m_d$. If $m_d > N$

$$g_t(\mathbf{s}(\mathbf{x})) = \begin{pmatrix} Q'_1(\mathbf{x}) \\ \vdots \\ Q'_N(\mathbf{x}) \\ 0 \\ \vdots \\ 0 \end{pmatrix} =: \mathbf{Q}^*(\mathbf{x})$$

g_t is invertible, which can be shown analogously to the case $N > m_d$. If $|R| = 1$, the map Ψ becomes

$$\Psi(\mathbf{y}) : \begin{cases} \mathbb{R}^{m_d} \rightarrow \mathbb{R} \\ \mathbf{y} \mapsto \frac{H_2}{H_1^2} \frac{(\Pi_1^{m_d} g_t^{-1} A_t^{-1} \mathbf{y})^2}{\Pi_2^{m_d} g_t^{-1} A_t^{-1} \mathbf{y}} \end{cases}$$

with

$$\begin{aligned} \frac{H_1^2}{H_2} \nabla \Psi(\mathbf{y}) &= 2 \frac{\Pi_1^{m_d} g_t^{-1} A_t^{-1} \mathbf{y}}{\Pi_2^{m_d} g_t^{-1} A_t^{-1} \mathbf{y}} \nabla (\Pi_1^{m_d} g_t^{-1} A_t^{-1})(\mathbf{y}) \\ &\quad - \frac{(\Pi_1^{m_d} g_t^{-1} A_t^{-1} \mathbf{y})^2}{(\Pi_2^{m_d} g_t^{-1} A_t^{-1})^2 \mathbf{y}} \nabla (\Pi_2^{m_d} g_t^{-1} A_t^{-1})(\mathbf{y}), \end{aligned}$$

where

$$\nabla (\Pi_1^{m_d} g_t^{-1} A_t^{-1})(\mathbf{y}) = \left((J_{g_t^{-1}}(A_t^{-1} \mathbf{y}))_1 A_t^{-1} \right)^T$$

and

$$\nabla (\Pi_2^{m_d} g_t^{-1} A_t^{-1})(\mathbf{y}) = \left((J_{g_t^{-1}}(A_t^{-1} \mathbf{y}))_2 A_t^{-1} \right)^T.$$

By $(J_{g_t^{-1}}(A_t^{-1} \mathbf{y}))_k$ we denote the k 'th row of the matrix $J_{g_t^{-1}}(A_t^{-1} \mathbf{y})$. Since there is at least one marker in the region R by assumption, we have for one $\mathbf{x} \in R$

$$S_1(\mathbf{x}) = s_1(\mathbf{x}) = \sum_{j=1}^{m_d} \beta_{1,j} Q_j(\mathbf{x}) = (g_t^{-1})_1(\mathbf{Q}^*(\mathbf{x})) > 0,$$

such that $s_2(\mathbf{x})$ is well defined:

$$\begin{aligned} s_2(\mathbf{x}) &= \frac{S_1(\mathbf{x}) - S_2(\mathbf{x})}{S_1(\mathbf{x})} \\ &= \frac{\sum_{j=1}^{m_d} \beta_{1,j} Q_j(\mathbf{x}) - \sum_{j=1}^{m_d} \beta_{2,j} Q_j(\mathbf{x})}{\sum_{j=1}^{m_d} \beta_{1,j} Q_j(\mathbf{x})} = (g_t^{-1})_2(\mathbf{Q}^*(\mathbf{x})). \end{aligned}$$

This yields

$$(J_{g_t^{-1}}(\mathbf{Q}^*(\mathbf{x})))_1 = (\beta_{1,1}, \dots, \beta_{1,N}, 0, \dots, 0)$$

and

$$(J_{g_t^{-1}}(\mathbf{Q}^*(\mathbf{x})))_2 = (\tilde{\beta}_1, \dots, \tilde{\beta}_N, 0, \dots, 0),$$

where

$$\tilde{\beta}_k = \frac{\beta_{1,k} - \beta_{2,k}}{\sum_{j=1}^{m_d} \beta_{1,j} Q_j} - \beta_{1,k} \frac{\sum_{j=1}^{m_d} \beta_{1,j} Q_j - \sum_{j=1}^{m_d} \beta_{2,j} Q_j}{\left(\sum_{j=1}^{m_d} \beta_{1,j} Q_j \right)^2}.$$

In particular, only the first N entries are non-zero. Therefore, multiplication with the matrix

$$A_t^{-1} = \begin{pmatrix} \tilde{A}_1 & \tilde{A}_2 \\ \tilde{A}_3 & \tilde{A}_4 \end{pmatrix}$$

with $\tilde{A}_2 = \mathbf{0} \in \mathbb{R}^{(m_d - N) \times N}$ yields again an element with zero-entries after the N -th component. Since the model bias vanishes if $N \leq m_d$, we find

$$\begin{aligned} F_t(s) &:= \mathbb{P} \left(\sqrt{t} (\hat{N}_R - N_R) \leq s \right) = \mathbb{P} \left(\sqrt{t} (\Psi(\hat{\mathcal{D}}) - \Psi(\mathcal{D})) \leq s \right) \\ &= \mathbb{P} \left(\sqrt{t} \nabla \Psi(\mathcal{D})^T (\hat{\mathcal{D}} - \mathcal{D}) + \frac{\sqrt{t}}{2} (\hat{\mathcal{D}} - \mathcal{D})^T \text{Hess}_{\Psi}(\tilde{\mathcal{D}}) (\hat{\mathcal{D}} - \mathcal{D}) \leq s \right), \end{aligned} \tag{A.5}$$

for an intermediate point $\tilde{\mathcal{D}}$. Since $\|\hat{\mathcal{D}} - \mathcal{D}\|_2 \leq \|\hat{\mathcal{D}} - \mathcal{D}\|_1$, where $\|\cdot\|_1$ and $\|\cdot\|_2$ denote the l^1 - and l^2 -norm on $\mathbb{R}^{|R|m_d}$, respectively, we find that

$$\mathbb{P}\left(\|\hat{\mathcal{D}} - \mathcal{D}\|_2^2 > \varepsilon\right) \leq \mathbb{P}\left(\|\hat{\mathcal{D}} - \mathcal{D}\|_1 > \sqrt{\varepsilon}\right) \leq 3 \exp(-t\varepsilon/25),$$

where the last inequality follows from Lemma 3 in Devroye (1983), using $m_d \leq 5 \log(t)$. Setting $\varepsilon = \log(t)/t \cdot 25$ gives

$$\mathbb{P}\left(\|\hat{\mathcal{D}} - \mathcal{D}\|_2^2 > \frac{25 \log(t)}{t}\right) \leq \frac{3}{t}.$$

By assumption of the theorem, there exists a positive constant $C > 0$ such that

$$|(\hat{\mathcal{D}} - \mathcal{D})^T \text{Hess}_{\Psi}(\tilde{\mathcal{D}})(\hat{\mathcal{D}} - \mathcal{D})| \leq C \|\hat{\mathcal{D}} - \mathcal{D}\|_2^2.$$

Hence, with F_t defined in (A.5), we find

$$F_t^-(s) \leq F_t(s) \leq F_t^+(s),$$

where

$$\begin{aligned} F_t^+(s) &:= \mathbb{P}\left(\sqrt{t} \nabla \Psi(\mathcal{D})^T (\hat{\mathcal{D}} - \mathcal{D}) \leq s + \frac{C\sqrt{t}}{2} \|\hat{\mathcal{D}} - \mathcal{D}\|_2^2\right) \\ &\leq \mathbb{P}\left(\sqrt{t} \nabla \Psi(\mathcal{D})^T (\hat{\mathcal{D}} - \mathcal{D}) \leq s + 25C \frac{\log(t)}{2\sqrt{t}}\right) + \frac{3}{t}, \end{aligned}$$

as well as

$$\begin{aligned} F_t^-(s) &:= \mathbb{P}\left(\sqrt{t} \nabla \Psi(\mathcal{D})^T (\hat{\mathcal{D}} - \mathcal{D}) \leq s - \frac{C\sqrt{t}}{2} \|\hat{\mathcal{D}} - \mathcal{D}\|_2^2\right) \\ &\geq \mathbb{P}\left(\sqrt{t} \nabla \Psi(\mathcal{D})^T (\hat{\mathcal{D}} - \mathcal{D}) \leq s - 25C \frac{\log(t)}{2\sqrt{t}}\right) - \frac{3}{t}, \end{aligned}$$

For given $v \in \mathbb{R}^{m_d}$ and $z \in \mathbb{R}$, the set

$$A_{v,z} = \{w \in \mathbb{R}^{|R|m_d} \mid v^T w \leq z\}$$

defines a closed half space in $\mathbb{R}^{|R|m_d}$ and as such, it is a 1-generated, closed convex set and we have

$$\mathbb{P}\left(\sqrt{t} \nabla \Psi(\mathcal{D})^T (\hat{\mathcal{D}} - \mathcal{D}) \leq s - \tau_t\right) = \mathbb{P}\left(\sqrt{t}(\hat{\mathcal{D}} - \mathcal{D}) \in A_{\Psi(\mathcal{D}), s - \tau_t}\right),$$

where $\tau_t = 25C \frac{\log(t)}{2\sqrt{t}}$. Note that we can write

$$(\hat{\mathcal{D}} - \mathcal{D}) = \frac{1}{t} \sum_{k=1}^t \left[\begin{pmatrix} I\{M_k(\mathbf{x}_{i_1}) = 0\} \\ \vdots \\ I\{M_k(\mathbf{x}_{i_1}) = m_d\} \end{pmatrix} - \begin{pmatrix} D_0(\mathbf{x}_{i_1}) \\ \vdots \\ D_{m_d}(\mathbf{x}_{i_1}) \end{pmatrix} \right] = \frac{1}{t} \sum_{k=1}^t \mathcal{M}_k,$$

where \mathcal{M}_k is defined in an obvious manner. It follows from Proposition 3 in Chernozhukov et al. (2017) that if the conditions M.1', M.2' and E.2' hold, where

$$(M.1') \quad \frac{1}{t} \sum_{j=1}^t \mathbb{E} \left(\frac{\nabla \Psi(\mathcal{D})^T}{\|\nabla \Psi(\mathcal{D})\|} \cdot \mathcal{M}_j \right)^2 \geq b \quad \text{for some positive constant } b,$$

$$(M.2') \quad \frac{1}{t} \sum_{j=1}^t \mathbb{E} \left| \frac{\nabla \Psi(\mathcal{D})^T}{\|\nabla \Psi(\mathcal{D})\|} \cdot \mathcal{M}_j \right|^{2+k} \leq B_t^k, \quad k = 1, 2,$$

$$(E.2') \quad \mathbb{E} \left[\exp \left(\left| \frac{\nabla \Psi(\mathcal{D})^T}{\|\nabla \Psi(\mathcal{D})\|} \cdot \mathcal{M}_j \right| / B_t \right) \right] \leq 2 \quad \forall j = 1, \dots, t,$$

we obtain

$$\begin{aligned} & \sup_{s \pm \tau_t \in \mathbb{R}} \left| \mathbb{P} \left(\sqrt{t}(\widehat{\mathcal{D}} - \mathcal{D}) \in A_{\Psi(\mathcal{D}), s \pm \tau_t} \right) - \mathbb{P} \left(\widetilde{Z} \in A_{\Psi(\mathcal{D}), s \pm \tau_t} \right) \right| \\ &= \sup_{s \in \mathbb{R}} \left| \mathbb{P} \left(\sqrt{t}(\widehat{\mathcal{D}} - \mathcal{D}) \in A_{\Psi(\mathcal{D}), s \pm \tau_t} \right) - \mathbb{P} \left(\widetilde{Z} \in A_{\Psi(\mathcal{D}), s \pm \tau_t} \right) \right| \\ &\leq C \left(\frac{B_t^2 \log(m_d |R| t)}{t} \right)^{\frac{1}{6}}, \end{aligned}$$

where $\widetilde{Z} \sim \mathcal{N}(0, \Sigma_R)$. We now show that conditions (M.1'), (M.2') and (E.2') are satisfied with $B_t = m_d^{\frac{3}{2}}$.

Verifying condition (M.1'):

Since the \mathcal{M}_k are i.i.d., we find

$$\frac{1}{t} \sum_{j=1}^t \mathbb{E} \left(\frac{\nabla \Psi(\mathcal{D})^T}{\|\nabla \Psi(\mathcal{D})\|} \cdot \mathcal{M}_j \right)^2 = \mathbb{E} \left(\frac{\nabla \Psi(\mathcal{D})^T}{\|\nabla \Psi(\mathcal{D})\|} \cdot \mathcal{M}_1 \right)^2.$$

Both $\nabla \Psi$ and \mathcal{M}_1 only have at most N non-zero entries (and N does not depend on t). Let $v_t \in \mathbb{R}^{m_d |R|}$, $\|v_t\| = 1$, be a deterministic vector. Then, if and only if the realizations of \mathcal{M}_1 are collinear on an event $\Omega_{0,t}$ with $\mathbb{P}(\Omega_{0,t}) \rightarrow 1$ as $t \rightarrow \infty$

$$\lim_{t \rightarrow \infty} \mathbb{E} \left[(v_t^T \mathcal{M}_1)^2 \right] = 0.$$

By assumption, there is at least one marker in the region R with individual brightness smaller than 0.5. Therefore, there exists a positive constant $\tilde{b} > 0$ such that $(D_0(\mathbf{x}), D_1(\mathbf{x})) \neq (0.5, 0.5)$ and $D_0(\mathbf{x}) \wedge D_1(\mathbf{x}) > \tilde{b}$. The first two components of the random vector \mathcal{M}_1 can either be

$$\mathbf{u}_1 := \begin{pmatrix} 1 - D_0(\mathbf{x}) \\ -D_1(\mathbf{x}) \end{pmatrix} \quad \text{or} \quad \mathbf{u}_2 := \begin{pmatrix} D_0(\mathbf{x}) \\ 1 - D_1(\mathbf{x}) \end{pmatrix}.$$

The probabilities for both events are bounded away from 0 as $t \rightarrow \infty$. Vectors \mathcal{M}_1 with first two components equal to \mathbf{u}_1 cannot be collinear to vectors \mathcal{M}_1 with first two components equal to \mathbf{u}_2 . To see this, let $\beta \in \mathbb{R}$. Then

$$\begin{pmatrix} 1 - D_0(\mathbf{x}) \\ -D_1(\mathbf{x}) \end{pmatrix} = \beta \begin{pmatrix} D_0(\mathbf{x}) \\ 1 - D_1(\mathbf{x}) \end{pmatrix}$$

iff

$$\beta = \frac{1 - D_0(\mathbf{x})}{D_0(\mathbf{x})} \quad \text{and} \quad \beta = \frac{D_1(\mathbf{x})}{1 - D_1(\mathbf{x})}.$$

The latter condition can only be satisfied if $(D_0(\mathbf{x}_j), D_1(\mathbf{x}_j)) = (0.5, 0.5)$. Therefore, at least one of the vectors containing either \mathbf{u}_1 or \mathbf{u}_2 is not perpendicular to v_t , such that condition (E.2') is satisfied. **Verifying condition (M.2'):**

We have that

$$\begin{aligned} \frac{1}{t} \sum_{j=1}^t \mathbb{E} \left| \frac{\nabla \Psi(\mathcal{D})^T}{\|\nabla \Psi(\mathcal{D})\|} \cdot \mathcal{M}_j \right|^{2+k} &= \mathbb{E} \left| \frac{\nabla \Psi(\mathcal{D})^T}{\|\nabla \Psi(\mathcal{D})\|} \cdot \mathcal{M}_1 \right|^{2+k} \\ &\leq \frac{\|\nabla \Psi(\mathcal{D})\|_1^{2+k}}{\|\nabla \Psi(\mathcal{D})\|_2^{2+k}} \leq (m_d |R|)^{\frac{2+k}{2}}. \end{aligned}$$

with $B_t = (m_d |R|)^{\frac{3}{2}}$.

Verifying condition (E.1’):

We need to show that

$$\mathbb{E} \left[\exp \left(\left| \frac{\nabla \Psi(\mathcal{D})^T}{\|\nabla \Psi(\mathcal{D})\|} \cdot \mathcal{M}_1 \right| / B_t \right) \right] \leq 2.$$

Since $\left| \frac{\nabla \Psi(\mathcal{D})^T}{\|\nabla \Psi(\mathcal{D})\|} \cdot \mathcal{M}_1 \right| \leq B_t^{1/3}$, condition (E.2’) trivially holds for sufficiently large t . Therefore, all three conditions are met and we obtain the following statement

$$\sup_{s \in \mathbb{R}} \left| \mathbb{P} \left(\sqrt{t}(\widehat{\mathcal{D}} - \mathcal{D}) \in A_{\Psi(\mathcal{D}), s + \tau_t} \right) - \mathbb{P} \left(\widetilde{Z} \in A_{\Psi(\mathcal{D}), s + \tau_t} \right) \right| \leq C \left(\frac{(m_d |R|)^3 \log(m_d |R|t)}{t} \right)^{\frac{1}{6}}.$$

Finally, we show that $\mathbb{P} \left(\widetilde{Z} \in A_{\Psi(\mathcal{D}), s + \tau_t} \right)$ and $\mathbb{P} \left(\widetilde{Z} \in A_{\Psi(\mathcal{D}), s} \right)$ are close, uniformly in s . Since $\widetilde{Z} \sim \mathcal{N}(0, \nabla \Psi(\mathcal{D})^T \Sigma_R \nabla \Psi(\mathcal{D}))$, it follows that

$$\sup_{s \in \mathbb{R}} \left| \mathbb{P} \left(\widetilde{Z} \in A_{\Psi(\mathcal{D}), s + \tau_t} \right) - \mathbb{P} \left(\widetilde{Z} \in A_{\Psi(\mathcal{D}), s} \right) \right| \leq \sup_{s \in \mathbb{R}} \left| \Phi \left(\frac{s}{\sigma_R} \right) - \Phi \left(\frac{s + \tau_t}{\sigma_R} \right) \right| \leq \frac{1}{\sqrt{2\pi}} \frac{\tau_t}{\sigma_R}.$$

Combining all previous steps yields

$$\sup_{s \in \mathbb{R}} \left| \mathbb{P} \left(\sqrt{t}(\widehat{N}_R - N_R) \leq s \right) - \mathbb{P} \left(\widetilde{Z} \in A_{\Psi(\mathcal{D}), s} \right) \right| \leq \widetilde{C} \left(\frac{1}{t} + \frac{\log(t)}{\sqrt{t}} + \left(\frac{(m_d |R|)^3 \log(m_d |R|t)}{t} \right)^{\frac{1}{6}} \right).$$

With $m_d \leq 5 \log(t)$ the claim of the theorem now follows. □

Acknowledgements

The authors want to thank Stefan W. Hell for helpful discussions. All authors gratefully acknowledge financial support by the DFG through CRC 755, project A07. F. W. is furthermore supported by the DFG via grant WE 6204/4-1.

References

- Aspelmeier, T., Egner, A., and Munk, A. (2015). Modern statistical challenges in high-resolution fluorescence microscopy. *Annu. Rev. Stat. Appl.*, 2:163–202.
- Balzarotti, F., Eilers, Y., Gwosch, K. C., Gynnå, A. H., Westphal, V., Stefani, F. D., Elf, J., and Hell, S. W. (2016). Nanometer resolution imaging and tracking of fluorescent molecules with minimal photon fluxes. *Science*, 355:606–612.
- Betzig, E., Patterson, G. H., Sougrat, R., Lindwasser, O. W., Olenych, S., Bonifacino, J. S., Davidson, M. W., Lippincott-Schwartz, J., and Hess, H. F. (2006). Imaging intracellular fluorescent proteins at nanometer resolution. *Science*, 313(5793):1642–1645.

- Chernozhukov, V., Chetverikov, D., and Kato, K. (2017). Central limit theorems and bootstrap in high dimensions. *Ann. Probab.*, 45(4):2309–2352.
- Coffman, V. C., Wu, P., Parthun, M. P., and Wu, J.-Q. (2011). Cenp-a exceeds microtubule attachment sites in centromere clusters of both budding and fission yeast. *J. Cell Biol.*, 185:563–572.
- Devroye, L. (1983). The equivalence of weak, strong and complete convergence in L_1 for kernel density estimates. *Ann. Statist.*, 11(3):896–904.
- Eggeling, C., Ringemann, C., Medda, R., Schwarzmann, G., Sandhoff, K., Polyakova, S., Belov, V. N., Hein, B., von Middendorff, C., Schönle, A., and Hell, S. W. (2009). Direct observation of the nanoscale dynamics of membrane lipids in a living cell. *Nature*, 457(7233):1159–1162.
- Engel, B. D., Ludington, W. B., and Marshall, W. F. (2009). Intraflagellar transport particle size scales inversely with flagellar length: revisiting the balance-point length control model. *J. Cell Biol.*, 187:81–89.
- Frahm, L., Keller-Findeisen, J., Alt, P., Schnorrenberg, S., del Álamo Ruiz, M., Aspelmeier, T., Munk, A., Jakobs, S., and Hell, S. W. (2019). Molecular contribution function in resolt nanoscopy. *Opt. Express*, 27(15):21956–21987.
- Gabitto, M. I., Marie-Nelly, H., Pakman, A., Pataki, A., Darzacq, X., and Jordan, M. I. (2021). A bayesian nonparametric approach to super-resolution single-molecule localization. *The Annals of Applied Statistics*, 15(4):1742 – 1766.
- Hell, S. W. (2007). Far-field optical nanoscopy. *Science*, 316(5828):1153–1158.
- Hell, S. W. and Wichmann, J. (1994). Breaking the diffraction resolution limit by stimulated emission: stimulated-emission-depletion fluorescence microscopy. *Opt. Lett.*, 19(11):780–782.
- Hohage, T. and Werner, F. (2016). Inverse problems with Poisson data: statistical regularization theory, applications and algorithms. *Inverse Problems*, 32(9):093001, 56.
- Hummer, G., Fricke, F., and Heilemann, M. (2016). Model-independent counting of molecules in single-molecule localization microscopy. *Mol. Biol. Cell*, 27:3637–3644.
- Klar, T., Jakobs, S., Dyba, M., Egner, A., and Hell, S. (2000). Fluorescence microscopy with diffraction resolution barrier broken by stimulated emission. *Proc. Natl. Acad. Sci. USA*, 97(15):8206–8210.
- Kulaitis, G., Munk, A., and Werner, F. (2021). What is resolution? A statistical minimax testing perspective on superresolution microscopy. *Ann. Statist.*, 49(4):2292–2312.
- Lee, S.-H., Shin, J. Y., Lee, A., and Bustamante, C. (2012). Counting single photoactivatable fluorescent molecules by photoactivated localization microscopy (palm). *Proc. Natl. Acad. Sci. USA*, 109(43):17436–17441.
- Masch, J.-M., Steffens, H., Fischer, J., Engelhardt, J., Hubrich, J., Keller-Findeisen, J., D’Este, E., Urban, N. T., Grant, S. G. N., Sahl, S. J., Kamin, D., and Hell, S. W. (2018). Robust nanoscopy of a synaptic protein in living mice by organic-fluorophore labeling. *Proceedings of the National Academy of Sciences*, 115(34):E8047–E8056.
- Meyer, F. (1994). Topographic distance and watershed lines. *Signal Process.*, 38:113–125.
- Munk, A., Proksch, K., Li, H., and Werner, F. (2020a). *Photonic Imaging with Statistical Guarantees: From Multiscale Testing to Multiscale Estimation*. Springer International Publishing, Cham.
- Munk, A., Staudt, T., and Werner, F. (2020b). *Statistical Foundations of Nanoscale Photonic Imaging*, page 125–143. Springer International Publishing, Cham.

- Park, M., Kim, H.-H., Kim, D., and Song, N. W. (2005). Counting the number of fluorophores labeled in biomolecules by observing the fluorescence-intensity transient of a single molecule. *Bull. Chem. Soc. Jpn.*, 78(9):1612–1618.
- Patel, L., Gustafsson, N., Lin, Y., Ober, R., Henriques, R., and Cohen, E. (2019). A hidden markov model approach to characterizing the photo-switching behavior of fluorophores. *The Annals of Applied Statistics*, 13(3):1397 – 1429.
- Proksch, K., Werner, F., and Munk, A. (2018). Multiscale scanning in inverse problems. *Ann. Statist.*, 46(6B):3569–3602.
- Rollins, G. C., Shin, J. Y., Bustamante, C., and Pressé, S. (2015). Stochastic approach to the molecular counting problem in superresolution microscopy. *Proc. Natl. Acad. Sci. USA*, 112(2):E110–E118.
- Sahl, S. J., Hell, S. W., and Jakobs, S. (2017). Fluorescence nanoscopy in cell biology. *Nat. Rev. Mol. Cell Bio.*, 18(11):685–701.
- Schmied, J. J., Gietl, A., Holzmeister, P., Forthmann, C., Steinhauer, C., Dammeyer, T., and Tinnefeld, P. (2012). Fluorescence and super-resolution standards based on DNA origami. *Nat. Methods*, 9(12):1133–1134.
- Staudt, T., Aspelmeier, T., Laitenberger, O., Geisler, C., Egner, A., and Munk, A. (2020). Statistical molecule counting in super-resolution fluorescence microscopy: towards quantitative nanoscopy. *Statist. Sci.*, 35(1):92–111.
- Ta, H., Keller, J., Haltmeier, M., Saka, S. K., Schmied, J., Opazo, F., Tinnefeld, P., Munk, A., and Hell, S. W. (2015). Mapping molecules in scanning far-field fluorescence nanoscopy. *Nat. Commun.*, 6:7977.
- Ta, H., Kiel, A., Wahl, M., and Herten, D.-P. (2010). Experimental approach to extend the range for counting fluorescent molecules based on photon-antibunching. *Phys. Chem. Chem. Phys.*, 12:10295–10300.
- Tang, W. and Tang, F. (2019). The poisson binomial distribution – old & new. *arXiv: Probability*.
- Westfall, P. H. and Young, S. S. (1993). *Resampling-based multiple testing: Examples and methods for p-value adjustment*, volume 279. John Wiley & Sons.
- Xie, Y., Shekhar, S., and Li, Y. (2022). Statistically-robust clustering techniques for mapping spatial hotspots: a survey. *ACM Comput. Surv.*, 55(2).